Cerebral Cortex, January 2018;28: 370–386

doi: 10.1093/cercor/bhx298
Advance Access Publication Date: 9 November 2017
Original Article

ORIGINAL ARTICLE

Effective Connectivity Measured Using Optogenetically Evoked Hemodynamic Signals Exhibits Topography Distinct from Resting State Functional Connectivity in the Mouse

Adam Q. Bauer[1], Andrew W. Kraft[2], Grant A. Baxter[1], Patrick W. Wright[1,3], Matthew D. Reisman[4], Annie R. Bice[1], Jasmine J. Park[1], Michael R. Bruchas[3,5,6], Abraham Z. Snyder[1], Jin-Moo Lee[1,2,3] and Joseph P. Culver[1,3,4]

[1]Department of Radiology, Washington University School of Medicine, Saint Louis, MO 63110, USA, [2]Department of Neurology, Washington University School of Medicine, Saint Louis, MO 63110, USA, [3]Department of Biomedical Engineering, Washington University School of Medicine, Saint Louis, MO 63110, USA, [4]Department of Physics, Washington University School of Medicine, Saint Louis, MO 63110, USA, [5]Department of Anesthesiology, Washington University School of Medicine, Saint Louis, MO 63110, USA and [6]Department of Neuroscience, Washington University School of Medicine, Saint Louis, MO 63110, USA

Address correspondence to Adam Bauer, Washington University School of Medicine, Scott McKinley Research Building, 4515 McKinley Ave, Saint Louis, MO 63110, USA. Email: aqbauer@wustl.edu

Abstract

Brain connectomics has expanded from histological assessment of axonal projection connectivity (APC) to encompass resting state functional connectivity (RS-FC). RS-FC analyses are efficient for whole-brain mapping, but attempts to explain aspects of RS-FC (e.g., interhemispheric RS-FC) based on APC have been only partially successful. Neuroimaging with hemoglobin alone lacks specificity for determining how activity in a population of cells contributes to RS-FC. Wide-field mapping of optogenetically defined connectivity could provide insights into the brain's structure–function relationship. We combined optogenetics with optical intrinsic signal imaging to create an efficient, optogenetic effective connectivity (Opto-EC) mapping assay. We examined EC patterns of excitatory neurons in awake, Thy1-ChR2 transgenic mice. These Thy1-based EC (Thy1-EC) patterns were evaluated against RS-FC over the cortex. Compared to RS-FC, Thy1-EC exhibited increased spatial specificity, reduced interhemispheric connectivity in regions with strong RS-FC, and appreciable connection strength asymmetry. Comparing the topography of Thy1-EC and RS-FC patterns to maps of APC revealed that Thy1-EC more closely resembled APC than did RS-FC. The more general method of Opto-EC mapping with hemoglobin can be determined for 100 sites in single animals in under an hour, and is amenable to other neuroimaging modalities. Opto-EC mapping represents a powerful strategy for examining evolving connectivity-related circuit plasticity.

Key words: cell-specific connectivity, effective connectivity, functional neuroimaging, optical imaging, optogenetics, resting state functional connectivity, structural connectivity

Introduction

Brain connectomics has emerged as a major focus of systems neuroscience research in health (van den Heuvel et al. 2016) and disease (Fornito et al. 2015). Connectomics, as originally conceptualized, referred to axonal connectivity, that is, white matter tracts, classically studied using histological methods (Jones 1999). More recently, the notion of connectomics has expanded to encompass resting state functional connectivity (RS-FC). RS-FC is defined in terms of temporally correlated intrinsic neural activity measured throughout the brain (Biswal et al. 1995; Raichle 2015). This correlated spontaneous activity defines widely distributed topographies known as resting state networks (RSNs) (Beckmann et al. 2005). Compared to task-based measures, RS-FC analyses have provided an efficient method for mapping the whole brain. The functional significance of RSNs derives from the observation that they topographically correspond to known sensory, motor, and "cognitive" functional systems (Smith et al. 2009; Power et al. 2011; Yeo et al. 2015). In humans, blood oxygen level dependent (BOLD) functional magnetic resonance imaging (fMRI) is the predominant technique used to study RS-FC (Damoiseaux et al. 2006; Biswal et al. 2010); diffuse optical tomography (DOT) provides an alternative method for measuring brain hemodynamics when fMRI is impractical (Liao et al. 2012; Ferradal et al. 2016) or medically precluded (Eggebrecht et al. 2014).

Attempts to explain RS-FC on the basis of known anatomical connectivity have been only partially successful (Damoiseaux and Greicius 2009; Honey et al. 2010). Thus, how RS-FC relates to anatomical connectivity remains incompletely understood. As a rule, functional connectivity is much broader than anatomical connectivity, most likely because temporally correlated intrinsic neural activity is generated within polysynaptic networks (Uddin 2013). Strong homotopic RS-FC between mirror loci across hemispheres (i.e., homotopic RS-FC) is a prominent feature across several species, including rodents (van Meer et al. 2010; Bero et al. 2012; Bauer et al. 2014; Otte et al. 2015), monkeys (Matsui et al. 2011), and humans (Stark et al. 2008). Discrepancies between homotopic RS-FC and structural connectivity have been especially noted in regions exhibiting high homotopic RS-FC strength. For example, while interhemispheric anatomical connectivity between left and right primary visual cortices in humans is sparse, homotopic RS-FC is strong (Vincent et al. 2007). And, following disconnection of direct (monosynaptic) callosal connections, homotopic RS-FC can still be observed (Uddin et al. 2008; 'Reilly et al. 2013), suggesting that interhemispheric RS-FC can be maintained through indirect (polysynaptic) pathways.

Effective connectivity (EC) represents a third type of connectivity intermediate between anatomical and functional connectivity that provides a measure of the influence (direct or indirect) that one brain region exerts over another (Friston et al. 1993). EC is therefore capable of revealing aspects of functional connectivity obscured by network-level synchronization. Unlike RS-FC analysis, measures of EC can reveal connection strength asymmetries between one brain region relative to another. In humans EC most commonly is studied using task-based fMRI (Friston 2011) in conjunction with sophisticated mathematical approaches, for example dynamic causal modeling or Granger causal modeling (Friston et al. 2013). More empiric strategies have used transcranial magnetic stimulation (Massimini et al. 2005) or even direct cortical stimulation in patients undergoing surgical evaluation (Matsumoto et al. 2004; Entz et al. 2014). In animals, EC most commonly is assessed invasively by delivering a stimulus (i.e., using current injected via microelectrodes (Ferezou et al. 2007; Histed et al. 2009; Matsui et al. 2011; Petkov et al. 2015; Chernov et al. 2016)) at one locus while measuring the physiological responses at different loci (Tolias et al. 2005; Premereur et al. 2016), or globally over the brain with fMRI (Matsui et al. 2012).

While hemoglobin provides endogenous contrast in the mammalian brain, imaging methods using hemoglobin alone (like fMRI) are limited in their ability to dissect subunits of a functional circuit. Both task-evoked responses and spontaneous hemodynamic fluctuations report ensemble activity spatially integrated over the neurovascular unit (Logothetis et al. 2001), and hence cannot distinguish between excitatory versus inhibitory processes within RSNs (Gibson et al. 1999; Yoshimura et al. 2005). A method for wide-field mapping of discrete neural circuits over the brain would provide for a more comprehensive view of the brain's structure–function relationship. Optogenetic (Opto) methods (Boyden et al. 2005; Alivisatos et al. 2013), which use activation of light-gated, opsin-expressing neurons (Wang et al. 2007), are a natural approach for dissecting brain circuitry within discrete subpopulations of neurons. Prior EC experiments in rodents using fMRI transfected cells with viral vectors to assess the physiological responses to stimulation in select sites (Lee et al. 2010; Desai et al. 2011). Compared to viral vector injections, the use of transgenic mice offers the advantage of more global expression and markedly increased flexibility as the site of stimulation can be easily controlled using mirrors (Ayling et al. 2009; Lim et al. 2012). Optical intrinsic signal imaging (OIS) allows for rapid wide-field recording of spontaneous (White et al. 2011; Bero et al. 2012; Bauer et al. 2014; Bumstead et al. 2016; Wright et al. 2017a) or induced (Grinvald et al. 1986; Frostig et al. 1990; Bouchard et al. 2009) hemodynamic fluctuations in the mouse brain. Here, we use optogenetic photostimulation in combination with OIS imaging in awake mice to create an Opto-EC mapping assay. In this sense of EC, causality is intrinsically a photostimulus leading to a (hemodynamic) response. Thus, the Opto-EC mapping strategy is more closely linked to EC mapping via direct electrical stimulation. We apply the general Opto-EC mapping method to mice expressing channelrhodopsin (ChR2) under control of a Thymocyte antigen-1 (Thy1) promoter to examine effective connections of cortical excitatory pyramidal neurons. To optimize the data collection for examining Thy1-based circuits, we titrated the photostimulation (frequency and duration, as in prior studies of rodent barrel cortex (Simons and Woolsey 1979; Grinvald et al. 1986; Dowling et al. 1996; McCasland et al. 1997)) to maximize the contrast-to-noise ratio (CNR) of responses to a single stimulation. Following optimization, we generated a set of Thy1-based EC (Thy1-EC) maps that explicitly reflect the influence of locally driven, Thy1-based excitatory activity on distant cortical regions connected to the site of stimulation. An inner-product operation is used to assess the magnitude of EC and is evaluated at zero-lag to simplify the comparison of Thy1-EC to conventional, zero-lag RS-FC. Because patterns of Thy1-EC exhibited higher spatial specificity compared to RS-FC maps, we hypothesized that patterns of Thy1-EC could more closely approximate local axonal projection connectivity (APC) than RS-FC. We tested this hypothesis by comparing both Thy1-EC and RS-FC data to histological data from the Allen Mouse Brain Connectivity (AMBC) Atlas.

Materials and Methods

Animals

Eleven male Thy1-ChR2-YFP mice (Stock number: 007612, The Jackson Laboratory) (Wang et al. 2007), and 6 male C57 mice

aged between 1 and 3 months were used for experimentation. The spatial distribution of ChR2 in the Thy1 mouse line used (line 18) has been well characterized in several previous studies. Within the brain, ChR2-positive cells include large pyramidal neurons in cortical layer 5, CA and CA3 pyramidal neurons in the hippocampus, mossy fibers in the cerebellum, and neurons in various regions of the thalamus, midbrain, and lower brainstem (Wang et al. 2007). Within the cortex, ChR2 is expressed in both axons and dendrites of the layer 5 pyramidal neurons, which have pronounced apical dendritic tufts in layers 1 and 2/3 (Thomson and Lamy 2007; Ayling et al. 2009). Within layer 5, ChR2 expression varies less than 50% across the anterior-posterior axis (Lim et al. 2012). Mice were given ad libitum access to food and water. All experimental protocols were approved by the Animal Studies Committee at Washington University in Saint Louis.

Animal Preparation

Mice were anesthetized with isoflurane (3% induction, 1% maintenance, 0.5 L/min air) and allowed 5–10 min for anesthetic transition. Each mouse was then placed on a heating pad maintained at 37 °C via feedback from a rectal probe (mTCII, Cell Microcontrols, Norfolk, VA, USA) and its head secured in a stereotactic frame. After shaving and cleaning the scalp, a midline incision was made along the top of the head to reflect the scalp, keeping the skull intact. A Plexiglas window with pretapped holes was installed over the skull and secured with dental cement (C&B-Metabond, Parkell Inc., Edgewood, NY, USA). A second, clear Plexiglas window covered the imaging window to prevent scratching while the mice were in their home cages. Together, the mass of the window, screws, and cover were less than 1 g. Once recovered (1–2 days), mice were behaviorally acclimated to the awake imaging system (Fig. 1A, see below) over a period of 5 days. On day 1, the acclimation procedure began by placing unrestrained mice on top of a levitating Styrofoam ball positioned under the imaging camera. Mice were allowed to freely walk on the ball for 10 min as a technician guided the ball to prevent the animal falling off. On days 2–5, an aluminum bracket was secured to the cranial window to restrict head movement, and the animal was placed on the levitating ball. With head movement restricted, mice were acclimated to the imaging system in 10-min sessions, 2 times per day. This protocol was repeated daily with increasing duration of head restraint until the animals exhibited no signs of stress and engaged in normal behavior (grooming, whisking, walking) while mounted in the imaging system. Mice prepared for collection of summed field potentials (see EEG Recording section below) underwent a similar procedure as above. Following scalp retraction, pilot holes were drilled into but not penetrating the skull at approximately −1 mm posterior to bregma, and +5 mm lateral to bregma (near barrel/auditory cortex), and over the cerebellum. Small stainless steel self-tapping screws (BASI Inc., Indiana, USA) were inserted into these holes for collecting EEG recordings. After installing the screws, a cranial window was secured to the skull with dental cement as described above.

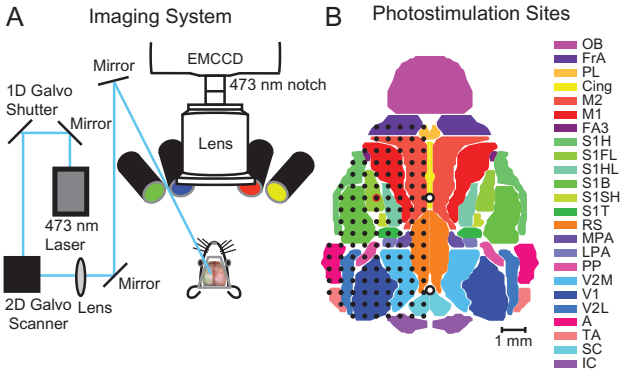

Figure 1. Mapping optogenetically defined effective connections in awake mice with OIS imaging. (A) Blue laser light (473 nm) is directed to the object plane of the imaging system by a set of broadband and galvanometer scanning mirrors and focused on the cortex by a lens. Four LEDs (centered at 470 nm, 530 m, 590 nm, and 625 nm) illuminate the dorsal surface of the mouse brain and are interleaved with the laser pulses. A 75 mm f/2.8 lens and back-illuminated EMCCD sensor collect diffuse light reflected from the skull. Prior to imaging, a small Plexiglas window glued to the intact mouse skull is used to secure the mouse head for imaging. (B) Sites (block dots) selected for photostimulation are separated by 500 microns and co-registered to the mouse brain prior to scanning using bregma and lambda as landmarks (White circles). The black dot with the red outline in left forepaw cortex represents the site used for photostimulus titration experiments (see Fig. 2). OB: olfactory bulb; FrA: frontal association; PL: prelimbic; Cing: cingulate; M2: secondary motor; M1: primary motor; FA3: frontal association area 3; S1H: primary sensory head; S1FL: primary sensory forelimb; S1HL: primary sensory hindlimb; S1B: primary sensory barrel; S1SH: primary sensory shoulder; S1T: primary sensory trunk; RS: retrosplenial; MPA: medial parietal association; LPA: lateral parietal association; PP: posterior parietal; V2M: secondary visual medial; V2L: secondary visual lateral; A: auditory; TA: temporal association; SC: superior colliculus; IC: inferior colliculus.

Imaging System

The awake mouse imaging system is a revised version of our previously published optical intrinsic signal imaging (OIS) system (White et al. 2011) modified to accommodate awake mouse imaging and free-space laser light delivery for photostimulation (Fig. 1A). Optical intrinsic signals are collected using 4 light emitting diodes (LEDs: 470 nm, M470L3-C1; 530 nm, M530L3-C1; 590 nm, M590L3-C1; 625 nm, M625L3-C1; Thorlabs, New Jersey, USA) illuminated sequentially and placed approximately 20 cm above the mouse's head. During imaging sessions, head-restrained mice are positioned on a Styrofoam ball (8″) levitated by pressurized air (30 psi), following methods outlined in Dombeck et al.(Dombeck et al. 2010). For collection of resting state data, the frame rate of the camera was approximately 118 Hz (camera exposure time was 0.0085 s). For the photostimulation titration experiments, the camera frame rate was 5× the laser stimulation frequency, corresponding to frame rates of 5 Hz (0.2 s exposure), 20 Hz (0.05 s), 50 Hz (0.02 s) and 100 Hz (0.01 s). The incident power of the 470 nm LED was 0.059 mW/mm^2, appreciably lower than the threshold for stimulating ChR2-expressing neurons by chance (1.3 mW/mm^2) (Mattis et al. 2011). EEG recordings (0.01 Hz to 5 kHz) collected over barrel cortex with and without the Blue LED in the imaging sequence verified that this light source did not alter the spectral content of electrical activity in the brain during the mapping experiments (Fig. S1).

For photostimulation, blue laser light (473 nm, BL473T-150, Shanghai Laser & Optics Century Company, Shanghai, China) is optically shuttered using a 1-D galvanometer, reflected off of 2 broadband mirrors, and delivered to the cortex by 2-D galvanometer scanning mirrors and periscope optics (Thorlabs). This laser light was aligned to the image plane of the EMCCD camera, and registered to each mouse using bregma and lambda as landmarks. Diffuse reflected light from the mouse head was detected by a cooled, frame-transfer EMCCD camera (iXon 897, Andor Technologies, Belfast, UK); the LEDs, laser and a camera were time-synchronized and controlled via a data acquisition

card (PCI 6733, National Instruments, Texas, USA) and computer (custom workstation, Dell, Texas, USA) using custom-written software (MATLAB, Mathworks, Massachusetts, USA). For all photostimulation experiments, it was important to interleave the laser stimulus with the frames of LED illumination to avoid corrupting OIS measurements at the site of stimulation. The illumination sequence was as follows: 470 nm LED, 530 nm LED, 590 nm LED, 625 nm LED, 473 nm laser, repeat. The laser frames were not used for hemoglobin decomposition. A 473 nm notch filter (ET405/473-488/NIRm, Chroma Technology, Vermont, USA) placed between the lens and camera prevented the laser from saturating the camera sensor during the short (5 ms) epochs of photostimulation in the laser frame. The passband characteristics of the notch filter were included as part of the spectroscopic inversion by multiplying each of the LED spectra by the transfer function of the filter.

Photostimulation

Blue laser light (473 nm, 0.5 mW, 5 ms pulses, effective spot size of 0.24 mm^2, continuous wave power density: 2.1 mW/mm^2) was used for all photostimulation studies. For optical titration experiments, different combinations of optical frequency (in Hz: 1, 4, 10, 20) and pulse train duration (in seconds: 1, 3, 10, 30) were delivered to left somatosensory forepaw cortex (Fig. 1*B*, black circle with red outline). Each combination of frequency and duration were delivered 6 times in blocks of 100 s (10 min per combination of stimuli). For the Thy1-EC mapping experiments, a rectilinear grid consisting of 180 points separated by 500 microns (19 points in the anterior-posterior direction and 11 points medial-laterally) was registered with each mouse using bregma and lambda as landmarks and scanned over the left hemisphere (approximately, 5 mm × 10 mm, Fig. 1*B*). The pattern of grid stimulation did not avoid potential overlap with surface vasculature mouse-to-mouse. To reduce scanning time, approximately 30 sites in the rectangular grid lying outside of the cortical surface were removed prior to imaging. For mapping, each photostimulus consisted of 22 s of rest, followed by 3 s of stimuli (473 nm light, 0.5 mW, 5 ms pulses delivered at 10 Hz). For each mouse, we randomized the order in which sites were stimulated to avoid potentially stimulating nearby sites during the hemodynamic refractory period. Functional responses (e.g., motor movements) were not observed following stimulation of any cortical region.

Imaging

Hemodynamic responses from titrated photostimuli were collected in 4, Thy1-ChR2 mice over 4 imaging sessions lasting 40 min each. For example, imaging session 1 consisted of 6 × 100 s blocks of 1 Hz stimuli to forepaw somatosensory cortex with 1, 3, 10, and 30-s stimulus trains. Thirty minutes of resting state data were collected in 8, Thy1-ChR2 mice during imaging session 5. In imaging sessions 6–9, Thy1-EC was mapped over the full grid in 5, Thy1-ChR2 mice (i.e., each mouse was mapped 4 times). Each of the 4 mapping sessions lasted approximately 75 min (180 grid sites × 25 s/site). Control photostimulation titration experiments were performed in 3 C57 mice using 10 Hz, 3 s stimuli delivered in 6 × 100 s blocks.

EEG Recording

EEG recordings were collected in 3 awake Thy1-ChR2 mice and 3 awake C57 mice over a frequency range of 0.01–5000 Hz using a differential amplifier (Dual Bio Amp connected to a Power Lab 16/35 digitizer, AD Instruments, Colorado, USA). The recording electrode was placed over the right barrel cortex with the reference electrode placed over the cerebellum. Electrical recordings were collected for 10 min in each mouse concurrently with sequential illumination of the LEDs. EEG traces were filtered using a second-order IIR notch filter set to 60 Hz. The spectral content was estimated using Welch's method with temporal windows overlapping by 50%. Two different window lengths were examined, 1 and 100 s. Spectra were normalized by their RMS power integrated over the lowest frequency to 50 Hz.

Image Processing

Image light intensity at each wavelength was interpreted using the Modified Beer-Lambert Law, usually expressed as: $\Phi(\mathbf{r},t) = \Phi_0{}^*\exp(-\Delta\mu_a(\mathbf{r},t)^*L)$. Here, $\Phi(\mathbf{r},t)$ is the measured light intensity, Φ_0 is the baseline light intensity, $\Delta\mu_a(\mathbf{r},t)$ is the change in absorption coefficient due to hemodynamic changes, and L is the optical path length factor for photons in the tissue (Arridge et al. 1992). We normalized relative to the average light intensity at each pixel over the imaging session, resulting in differential measures of absorption at each wavelength at each pixel: $\Delta\mu_{a,\lambda}(\mathbf{r},t) = -\ln(\Phi_\lambda(\mathbf{r},t)/\langle\Phi_{0\lambda}(\mathbf{r},t)\rangle)/L_\lambda$. Absorption coefficient data were converted to hemoglobin (Hb) concentration changes by inverting the system of equations, $\Delta\mu_{a,\lambda}(\mathbf{r},t) = E_{\lambda,i}\,\Delta[Hb_i](\mathbf{r},t)$ (where E is the extinction coefficient matrix (Prahl 2002), and i runs over hemoglobin species). This inversion was performed using least-squares methods, yielding changes in oxygenated hemoglobin (HbO) and deoxygenated hemoglobin (HbR) at each pixel at each time point. Total hemoglobin was calculated as the sum of HbO and HbR. For evoked stimuli, differential changes in hemoglobin concentration were filtered from 0.009 Hz to 0.5 Hz, and resting state data were filtered from 0.009 to 0.08 Hz following previous fcOIS reports (White et al. 2011; Bero et al. 2012; Bauer et al. 2014). After filtering, each pixel's time series was down-sampled to 1 Hz, and all further analysis was performed only on those pixels labeled as brain using a manually constructed brain mask. Image sequences of each mouse (as well as the brain mask for each mouse) were affine-transformed to a common atlas space following our previously published protocols (Bauer et al. 2014). The intersection of every brain mask (and optogenetic mapping grids) were calculated so that all subsequent comparisons were performed on shared brain regions across all mice. In total, 95 sites for photostimulation were shared across all mice.

Functional/Effective Connectivity Measures

To investigate the strength of functional network connections, each site of photostimulation (determined by maximum laser intensity in each laser frame) served as a "seed location" for both RS-FC analysis and Thy1-EC analysis. Resting state and phototimulus-evoked time traces were calculated by averaging the time traces within 0.25 mm of a seed locus (approximately 30 pixels) during either the resting state or optogenetic mapping scans. RS-FC maps were calculated by zero-lag correlation of spontaneous activity at each seed location with the spontaneous activity in every pixel in the brain. Thy1-EC maps were created by zero-lag correlation of the photostimulus-evoked time course at each seed location with the activity in every other pixel during the stimulated epoch (25 s). Each site of photostimulation on the left hemisphere (stimulus sites) was reflected about midline onto the right hemisphere, and all left

and right hemisphere grid points were used as recording sites. Thy1-EC matrices were constructed by evaluating the zero-lag correlation between photostimulus-evoked responses at each stimulated site and activity at each recording site. RS-FC matrices were created by evaluating the zero-lag correlation in spontaneous activity at the coordinates of each stimulated site with the spontaneous activity at each recording site. Average network connectivity was determined by calculating the mean Fisher z-transformed Pearson correlation ($z(r)$) within each element of the site-site connectivity matrix. Asymmetry in the average Thy1-EC matrix was determined in the ipsilateral (left) hemisphere by subtracting the upper diagonal from the lower diagonal. All results are reported for total hemoglobin unless otherwise stated because this contrast provides the highest CNR and has been shown to provide more focal activity (Culver et al. 2005).

Comparisons to Mouse Brain Anatomical Connectivity

In order to determine how the functional maps (Thy1-EC and RS-FC) relate to underlying axonal projection connectivity (APC), we collected images from the Allen Mouse Brain Connectivity (AMBC) Atlas (http://connectivity.brain-map.org/, last accessed 20 October 2017 (Lein et al. 2007; Oh et al. 2014)) using the source search feature within the Mouse Connectivity Data Portal and the cortical map signal viewer. These images report enhanced green fluorescent protein (EGFP)-labeled axonal projections of sites injected with a pan-neuronal adeno-associated virus under a human synapsin I promoter in wild-type (C57BL/6J) mice (Oh et al. 2014). Thus, these tracer studies represent monosynaptic connections originating from the site of injection. We selected APC images based on the proximity of the sites of viral injection to those used for interrogation in the OIS data. The cortical map signal viewer was used to produce projection images of all EGFP-labeled cortical axons. Projection images were registered to OIS data using bregma, lambda, and barrel cortex as landmarks, and restricted to the same field of view as the OIS dataset. Each APC image was normalized by its maximum fluorescence intensity prior to analysis.

Statistics

Levels of significance ($P < 0.05$) for all pair-wise comparisons were determined using a 2-tailed Students t-test assuming unequal group variance (Matlab). When applicable, Bonferroni correction was used to correct for alpha inflation due to multiple comparisons. All analyses conducted and visualizations generated were executed in Matlab (Mathworks).

Results

Titrating Optical Stimuli

Preliminary experiments were performed to calibrate the dose-response curve of ChR2-evoked hemodynamic responses (ChR2-HRs) and to ensure stability of the mapping procedure. To this end, laser stimulation was applied to the forepaw region of somatosensory cortex in 4 awake animals (Fig. 1B, red circle). These experiments established that the mapping procedure met the following criteria: 1) low power (<1 mW) optical stimulation to avoid tissue heating (Christie et al. 2013; Rungta et al. 2017); 2) non-saturating dose-response regime (Sheth et al. 2004); 3) rapid decay of responses to baseline to enable efficient sequential scanning; and 4) high CNR.

Cortical responses of oxygenated (HbO), deoxygenated (HbR) and total hemoglobin (HbT) were measured with fixed optical power (0.5 mW) and a pulse width (5 ms) over an effective spot size of 0.24 mm^2 (2.1 mW/mm^2). This intensity corresponds to a beam diameter of 0.55 mm (calculated using the full-width at half max (FWHM) of the laser spot diffusely reflected from the skull/brain and detected by the camera). This value is slightly higher than the effective power density required to activate 50% of neurons (EPD50) expressing wild-type ChR2, which is 1.3 mW/mm^2(Mattis et al. 2011). Frequency and duration were systematically varied at approximately log-spaced intervals. ChR2-HRs monotonically increased as a function of both stimulus frequency (Fig. 2A, columns) and stimulus duration (Fig. 2A, rows). In greater detail, for stimulus train durations of 3 s, ChR2-HRs increased in magnitude as a function of increasing stimulus frequency up to 10 Hz, then plateaued at 20 Hz (Fig. 2B, top row). Interestingly, this response profile was not observed in experiments varying stimulus duration with fixed frequency (Fig. 2B, bottom row). Two distinct ChR2-HRs emerged in responses to stimuli lasting 10 s or longer (Fig. 2B, bottom row). The faster response peaked within 2–3 s after which a slower, high amplitude (nearly twice that of the early response), secondary ChR2-HR emerged with a peak time approximately equal to the stimulus duration. Interestingly, while HbO and HbT generally increased in amplitude with increasing stimulus duration, HbR amplitude remained relatively stable. To examine if these ChR2-HRs were unique to the somatosensory region, the same set of titration experiments were performed in retrosplenial cortex (Fig. S2). As in the responses to the forepaw region, we observed fast responses to stimulus trains of short duration, and both fast and slow responses for long stimulus trains. These commonalities indicate an approximately uniform response profile over the cortex to the same set of stimulus parameters.

ChR2-HRs of HbT in forepaw cortex were further characterized in terms of peak response magnitude as well as integrated area under the response curve (AUC) (Fig. 2C–F). As a function of stimulus duration, AUC of HbT linearly increased between 1 Hz and 10 Hz, then partially saturated at 20 Hz. Rapid sequential stimulation experiments require a quick decay of the peak response to baseline (Devor et al. 2003). As illustrated in Figure 2B, the shortest stimulus trains took approximately 2.5 s to return to 50% of their maximum amplitude, while longer train durations took approximately 2–5 times longer (Fig. 2G). Thus, long-duration stimulus trains (10 s or greater) and high stimulus frequencies (20 Hz or greater) are not well suited to mapping, owing to emergence of a slow component (Fig. 2B, 10 Hz, >10 s), saturation (>10 Hz, 3 s), or extended response duration (Fig. 2G). Accordingly, for mapping we used 5 ms optical stimuli delivered at 10 Hz for 3 s (0.5 mW, 0.075 mJ, 473 nm light). When stimulating forepaw somatosensory cortex with this laser stimulus, we observe hemodynamic responses with a FWHM diameter of 1.4 mm (1.6 mm^2), approximately 3× larger than the spot size of the laser. The spatial extent of our measured response aligns well with the spatial extent of hemodynamic responses in forepaw cortex following either peripheral or optogenetic stimulation (Desai et al. 2011; Kahn et al. 2011; Scott and Murphy 2012; Vazquez et al. 2014; Iordanova et al. 2015). Single presentations using these parameters provided robust cortical responses with sufficient CNR to adequately unmix the contribution of HbO, HbR, and HbT in individual mice (Fig. 2H, Fig. S3). HbT generally provided the highest CNR across all 3 contrasts and therefore was evaluated in all mapping experiments. These mapping photostimuli did not elicit detectable HRs in control mice (Fig. S4).

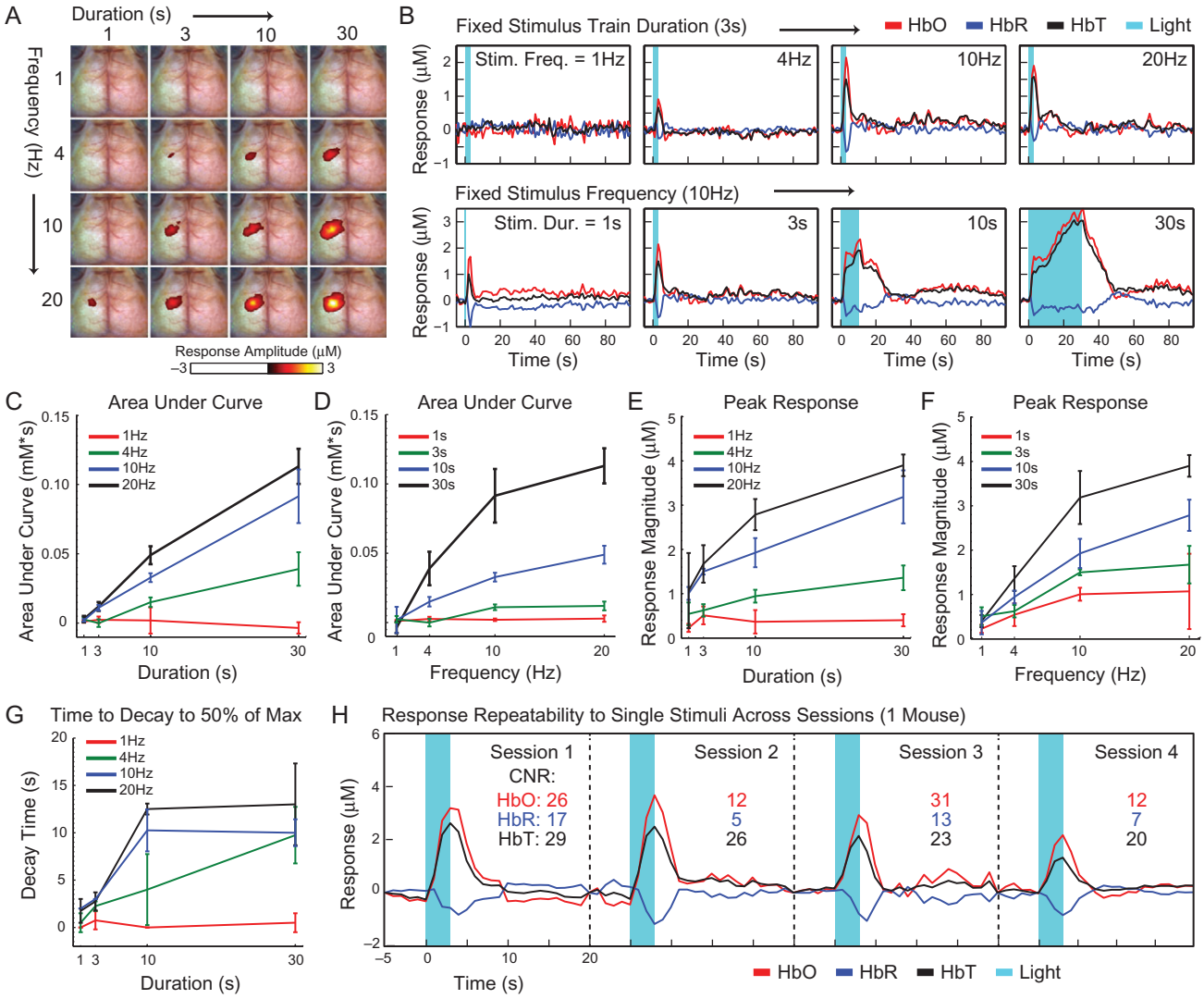

Figure 2. ChR2-evoked hemodynamic responses depend on photostimulation parameters. (*A*) Maps of total hemoglobin at peak response show increasing response magnitude and activation area for increasing stimulus frequency (rows) or increasing stimulus duration (columns). All images show only those pixels containing a response magnitude greater than 0.5 μM. (*B*) ChR2-evoked time courses of oxygenated (HbO), deoxygenated (HbR), and total (HbT) hemoglobin following photostimulation. Top row: fixed duration with increasing stimulus frequency Bottom row: fixed frequency with variable duration. Stimulus trains of 10 s or more produced an initial, fast response followed by a slower response that takes longer to reach peak magnitude and return to baseline. The ChR2-evoked responses of HbT in panel (*B*) were quantitatively assessed to determine which photostimuli would be ideal for rapidly mapping optogenetically defined, Thy1 circuits over the cortex. Ideal stimuli should produce a large response magnitude that quickly returns to baseline. Characteristics of the hemodynamic response included area under the curve as a function of (*C*) stimulus duration or (*D*) stimulus frequency, as well as the peak response magnitude as a function of (*E*) stimulus duration or (*F*) stimulus frequency. (*G*) Time measured for maximum response to decay to 50% of peak. A response had to be greater than 0.5 μM to be included in the decay calculation, thus the lack of error bar for the 1 Hz, 10 s duration data. (*H*) Responses to single presentations of 10 Hz, 3 s stimuli in 1 mouse. After optimization, ChR2-HRs are repeatable in an individual mouse across 4 separate imaging sessions. Generally, HbT produced hemodynamic responses with the greatest contrast-to-noise across sessions and was used for all mapping experiments. All stimuli were performed with 5 ms pulses of 473 nm, 0.5 mW laser light. All responses in panels (*A*–*G*) were calculated by averaging 6 presentations of each combination of stimuli over 4 mice. Error bars represent standard deviation from the mean.

Mapping Thy1-based Effective Connections with Hemoglobin

Single photostimuli were presented at cortical locations defined by a 500 micron × 500 micron grid over the left hemisphere (Fig. 1*B*) in 5 mice. Responses were recorded from t = –5 to 20 s relative to stimulus onset in all pixels in the brain. These data were organized into a 3-dimensional matrix (pixels × time × seed location) and analyzed in several ways. First, we examined peak ChR2-HR at each site (Fig. S3*B*, select maps shown in Fig. S5). Increased blood volume was observed at each site following laser stimulation; changes in HbT ranged from 0.02% to 2.4% with a mean of 1.06% over all sites stimulated in the left hemisphere. Of the 95 sites shared in common across mice, 80 locations (84% of sites) exhibited a CNR greater than 3 (Fig. S3*B*), confirming that the stimulus parameters were sufficient for wide-field mapping. Optogenetically defined effective connectivity of Thy1 circuits (Thy1-EC) was calculated in each animal by correlating the 25-s long-evoked ChR2-HR at the stimulated grid point with each pixel's 25-s long time course over the same epoch (Fig. 3, Thy1-EC). Local EC was observed within a radius of ~500 microns surrounding each stimulated site. Distant (>3 mm from the stimulated site) ipsilateral responses were observed in somatosensory and motor regions.

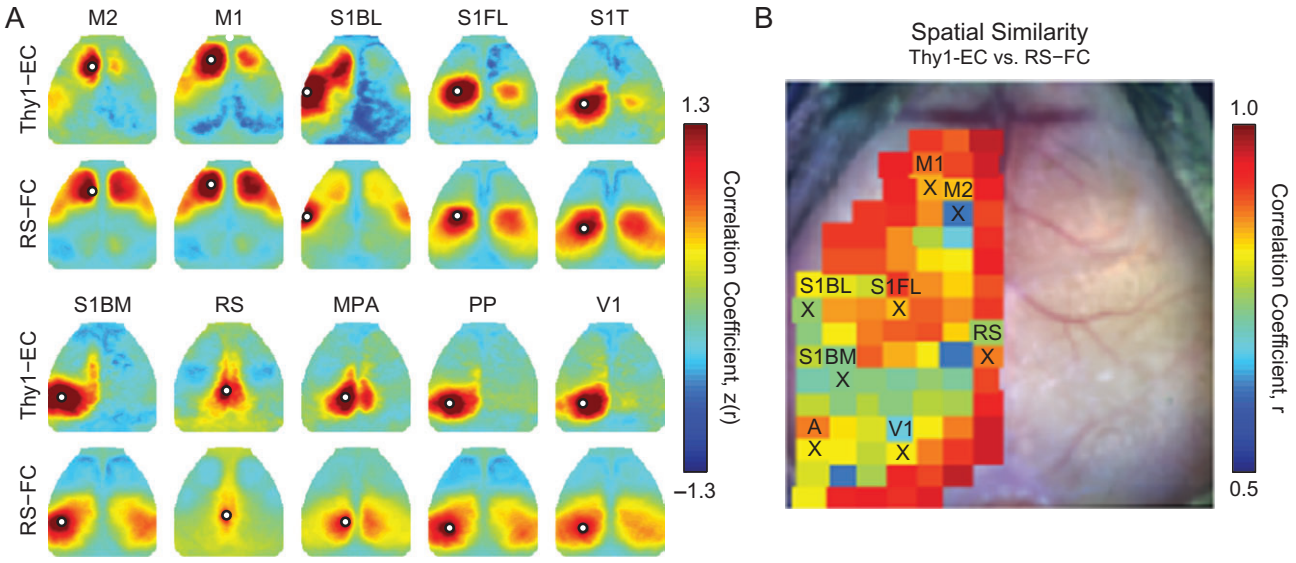

Figure 3. Mapping effective connectivity of excitatory neurons using hemoglobin-based contrast. (*A*) Thy1-EC: Maps of Thy1-based effective connectivity in 5 mice calculated by zero-lag correlation of the evoked time course at the stimulated site and activity in each brain pixel during that epoch (25 s). RS-FC: Resting state functional connectivity maps in 8 mice calculated by zero-lag correlation of spontaneous time courses at the coordinates of stimulated sites and the rest of the brain (20–30 min) during a separate imaging session. All images are maps of total hemoglobin. (*B*) Map of spatial similarity following normalized spatial dot product of the Thy1-EC and RS-FC maps of A. Within the similarity maps, red values indicate more similar connectivity structure across modalities, while blues indicate more disparate connectivity structure. Sites labeled with an "X" are evaluated against ex-vivo axonal projection connectivity in Fig. 6. M2: secondary motor; M1: primary motor; S1BL: primary somatosensory barrel (lateral); S1FL: primary somatosensory forelimb; S1T: primary somatosensory trunk; S1BM: primary somatosensory barrel (medial); RS: retrosplenial; MPA: medial parietal association; PP: posterior parietal; V1: primary visual; A: auditory.

For example, stimulation of primary motor cortex revealed EC with the medial barrel field in primary somatosensory cortex (S1BM); likewise, stimulation of secondary motor cortex revealed EC with the lateral barrel field (S1BL) (Fig. 3*A*, Thy1-EC). Homotopic EC (response in the contralateral hemisphere) was observed in primary and secondary motor cortex (M1 and M2), forelimb somatosensory (S1FL), retrosplenial (RS), and medial parietal association (MPA) cortices, but was not observed in medial barrel cortex (S1BM), visual (V1), posterior parietal (PP), and auditory cortices. Patterns of Thy1-EC were highly reproducible within and across mice over the 4 mapping sessions (Fig. S6). The average spatial similarity (normalized image dot product) of individual Thy1-EC maps compared to the group-averaged maps was $r = 0.74 \pm 0.09$ (mean + standard deviation). Thy1-EC mapping with HbO (Fig. S7) generally produced topographically similar maps to those of HbT, while mapping with HbR (Fig. S8) produced maps that qualitatively appeared less spatially specific than those of HbO and HbT. Thy1-EC maps from HbO and HbR were not further analyzed.

Thy1-EC Maps Exhibit Topography Distinct from RS-FC Maps

In contrast to the evoked activity used for Thy1-EC mapping, resting state functional connectivity (RS-FC) reflects spontaneous coherent activity across many cell populations. Thus, Thy1-EC and RS-FC maps may differ. To examine such differences, spontaneous hemodynamic activity was recorded for 30 min in a separate imaging session in 8 awake mice. Following previously published protocols (White et al. 2011), RS-FC was calculated as the Pearson correlation of intrinsic activity using the coordinates of every stimulated site as a seed region. Pearson correlations were Fisher z-transformed prior to display as RS-FC maps (Fig. 3*A*, RS-FC). While both maps shared common features, the RS-FC maps were both qualitatively and quantitatively different from their Thy1-EC counterparts. For example, stimulation of M2 demonstrated ipsilateral EC with barrel cortex (M2 to S1BL, $z(r) = 0.45$) in the Thy1-EC map, (Fig. 3*A*, M2) that was not present in the RS-FC map (M2 to S1BL, $z(r) = 0.02$; $P = 0.021$). Despite the different topography between the Thy1-EC maps of motor cortex (M1, M2, Fig. 3*A*), RS-FC maps in those same regions were nearly identical. Further, RS-FC maps were largely bilaterally symmetric. The mean spatial similarity between the left and right hemispheres across all RS-FC maps, evaluated as Pearson *r*, was 0.92; significantly less bilateral symmetry was observed in the regional Thy1-EC maps (Pearson $r = 0.59$; a *t*-test of bilateral symmetry in RS-FC and Thy1-EC across all mice produced a $P < 1e{-}6$).

The topographical similarity between the RS-FC and Thy1-EC was quantified by evaluating the spatial correlation between maps obtained at each interrogated site (Fig. 3*B*). Here, red and blue values indicate greater or lesser topographical similarity, respectively. The map of cross-method similarity shows substantial variation depending on seed site (representative regions labeled with an "X" in Fig. 3*B* are evaluated further in Fig. 6). The greatest disparity between RS-FC and Thy1-EC maps occurs in M2, lateral and posterior regions of the somatosensory cortex (e.g., S1BL, S1BM), parietal, and visual regions.

Homotopic Connectivity in RS-FC and Thy1-EC Maps of Awake Mice

To facilitate visualization of connectivity over the entire field of view, the coordinates of each photostimulation site in the left hemisphere were reflected about midline, and all left (ipsilateral) and right (contralateral) grid points were treated as recording

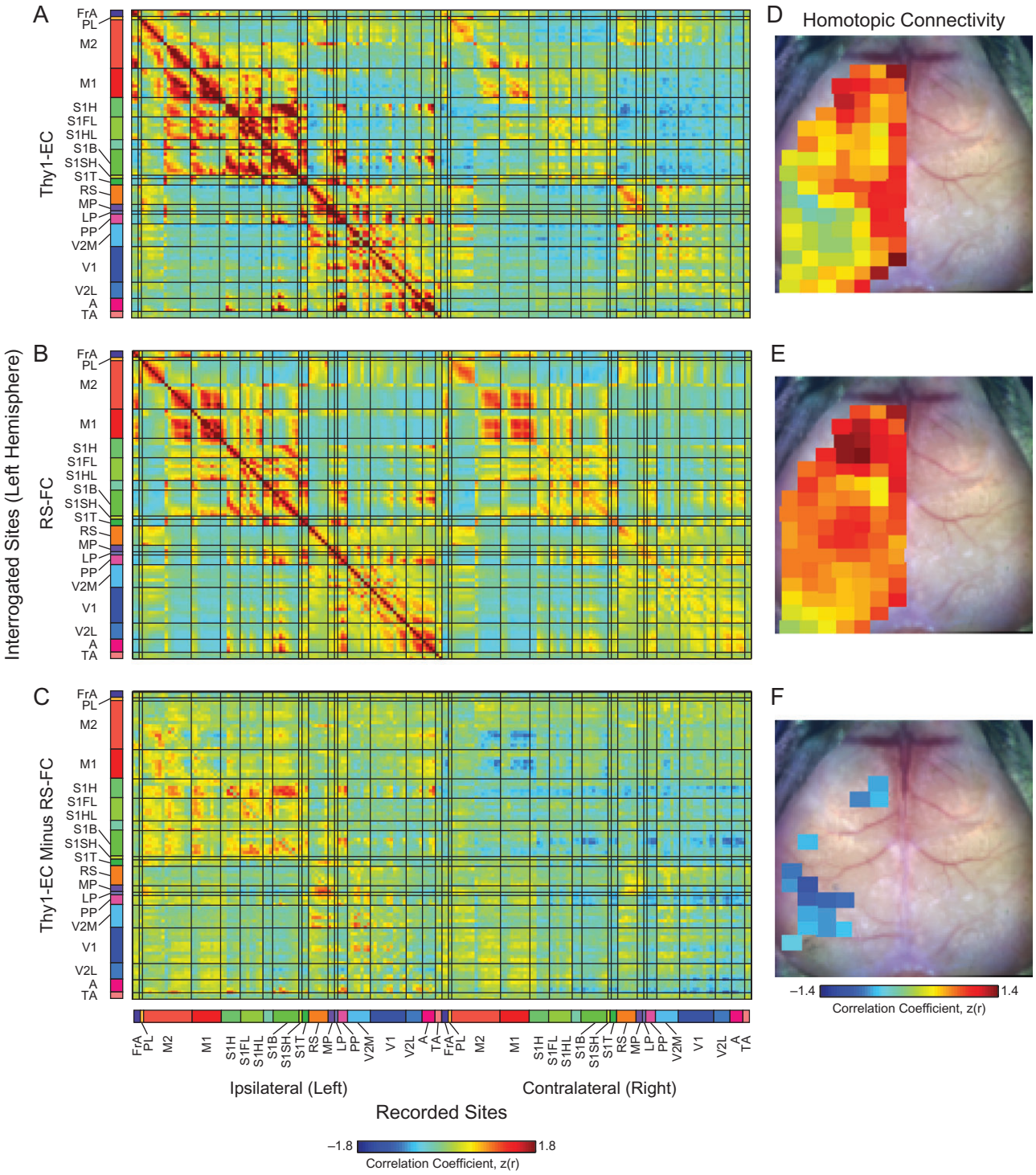

Figure 4. Site-wise connectivity structure across both the (*A*) Thy1-EC (5 mice) and (*B*) RS-FC (8 mice) mapping methods. Matrices report group-averaged connectivity; rows represent sites (95 total) chosen for optogenetic targeting (Thy1-EC) or resting state analysis (RS-FC), columns represent recording sites determined by coordinates in the left ipsilateral hemisphere chosen for photostimulation, and those same coordinates reflected about midline to the contralateral right hemisphere (190 in total). The color code for each functional assignment is defined in Fig. 1*B*, and the size of each region reflects its spatial extent within our field of view. (*C*) Difference matrix shows widespread differences in ipsilateral connectivity, as well as large differences in connection strength with contralateral cortex. Site-wise homotopic connectivity (off diagonal on right side of matrix in *A*) in the (*D*) Thy1-EC and (*E*) RS-FC datasets. (*F*) The strongest regional differences in connection strength between homotopic sites occured in motor, posterior regions of somatosensory, and parietal cortices. Differences in homotopic connectivity were thresholded at a corrected *P*-value of $0.05/95 = 5.3 \times 10^{-4}$.

sites. Effective and functional connectivity were evaluated for all ROI pairs (Fig. 4). For both methods, the connectivity matrices are organized such that the rows represent interrogated sites (stimulated for Thy1-EC (Fig. 4*A*) or a seed ROI for RS-FC (Fig. 4*B*)) and columns represent recording sites. The pixels are ordered, first, by hemisphere, then functional region. The "Ipsilateral"

matrix shows connectivity within the left hemisphere; the "Contralateral" matrix shows connectivity between the right and left hemispheres. The matrices reveal certain features common to both methods: Positive ipsilateral correlations are evident near sites investigated, and anticorrelations between anterior and posterior regions. These results appear as reds and oranges along the ipsilateral (left) diagonal and as blues in the off-diagonal blocks, respectively. Thy1-EC versus RS-FC differences are shown in Figure 4C. Thy1-EC exhibited significantly greater ipsilateral connectivity between somatosensory and motor regions ($z(r) = 0.50$) as compared to RS-FC ($z(r) = 0.30$; $P = 0.018$). This result appears as reds and oranges in the "Ipsilateral" difference matrix of Figure 4C. Conversely, Thy1-EC exhibited significantly lower interhemispheric connectivity ($z(r) = 0.56$) compared to RS-FC ($z(r) = 0.76$; $P = 1.7e{-}5$). This result appears as blues in the "Contralateral" difference matrix in Figure 4C.

Strong homotopic functional connectivity (between mirror loci of both hemispheres) is a prominent feature of RS-FC in the anesthetized mouse brain (Bero et al. 2012; Bauer et al. 2014). Homotopic connections appear on the main diagonal of the "Contralateral" matrix of Figure 4A–C. Figure 4D–F shows homotopic connectivity rendered on the left hemisphere. Each pixel represents $z(r)$ evaluated between homologous regions in both hemispheres, treating each pixel in the left hemisphere either as a site of stimulation (Thy1-EC data, Fig. 4D) or a seed region (RS-FC data, Fig. 4E). Generally positive homotopic connectivity is evident in the results obtained by both methods. A region of relatively low homotopic Thy1-EC is evident at the boundary between somatosensory cortex and parietal regions. Compared to RS-FC, significantly lower homotopic Thy1-EC was observed in motor ($z(r) = -0.62$), barrel ($z(r) = -1.00$) and head ($z(r) = -0.56$) regions of somatosensory cortex, lateral parietal regions ($z(r) = -0.84$), visual ($z(r) = -0.64$), and auditory cortex ($z(r) = -0.41$) (Fig. 4F, Thy1-EC minus RS-FC; connectivity differences shown for Bonferroni adjusted P-value of $P = 0.00053$ for 95 comparisons across mice). The reduced homotopic Thy1-EC in these regions was observed despite large ChR2-induced responses at those locations (Fig. S3B). Conversely, many regions exhibiting strong homotopic Thy1-EC about the midline (e.g., retrosplenial, cingulate, secondary motor) exhibited relatively weak responses to direct stimulation (Fig. S3B). These findings suggest that heterogeneity in homotopic Thy1-EC magnitude is not attributable to insufficient CNR at a given site or differences in ChR2 expression levels over the cortex.

The presence/absence of ipsilateral or homotopic Thy1-EC over the cortex could also depend on the choice of stimuli. While the left hemisphere was not mapped with different stimulus parameters, the titration data in forepaw somatosensory cortex provide 1 cortical region for examining how homotopic Thy1-EC magnitude relates to stimulus duration. For the 10 Hz stimulus titration experiment, we calculated Thy1-EC for stimulus durations of 1, 3, 10, and 30 s (Fig. S9A). Interestingly, the 10 s duration stimuli exhibit significantly reduced homotopic EC compared to the 3 and 30 s stimulus train durations for both HbO and HbT (Fig. S9B), indicating reduced temporal coherence between left and right signals within the forepaw region.

Asymmetry in Thy1-EC Maps

Functional connectivity is an inherently symmetric relation. Thus, given 2 regions A and B, by definition, FC(A,B) = FC(B,A). In contrast, effective connectivity may be asymmetric. Thus, EC (A→B) might not equal EC(B→A). We evaluated the spatial dependence of asymmetry of Thy1-EC (Fig. 5), confining the analysis to the left hemisphere. Asymmetry of Thy1-EC was most prominent in somatic sensory and motor regions (Fig. 5A). For example, between the primary motor cortex (M1) and the lateral barrel region of somatosensory cortex (S1BL) we found Thy1-EC (M1→S1BL): $z(r) = 0.41$ and Thy1-EC(S1BL→M1): $z(r) = 1.49$. Thus, sensory→motor EC was greater than motor→sensory EC by a factor of 2.64 ($P < 1e{-}6$). To isolate the asymmetric component of pair-wise Thy1-EC, the upper triangle of Figure 5A was subtracted from the lower triangle; the result reports the average asymmetry in intra-hemispheric effective connectivity (Fig. 5B). With respect to the functional assignments along the rows, reds indicate stronger outgoing connectivity to columns; blues indicate stronger incoming connectivity from columns. Inspection

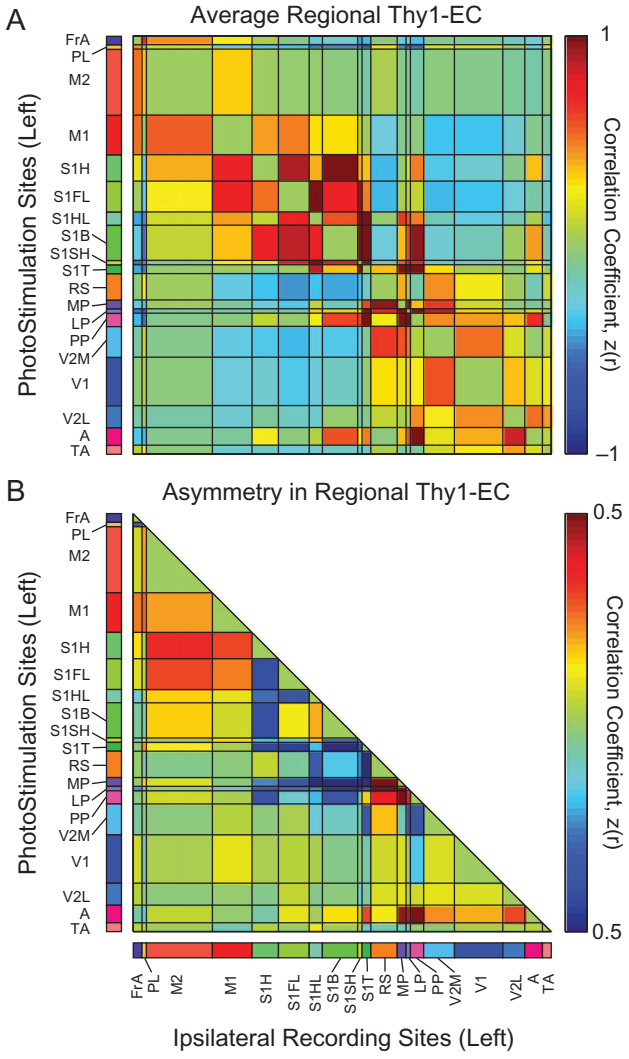

Figure 5. Hemodynamic mapping of Thy1-EC reports connection strength asymmetry between reciprocal sites. (A) Effective connectivity in the ipsilateral hemisphere of the Thy1-EC matrix in Fig. 4A averaged within each functional region. Rows are sites stimulated while columns are sites recorded in the ipsilateral hemisphere. Disparity in connectivity magnitude above and below the diagonal denotes an imbalance in connectivity strength between network pairs. (B) Asymmetry in connectivity strength calculated by subtracting the upper triangle of the average connectivity matrix in (A) from the lower triangle and plotting the differences. Reds indicate the stimulated network has stronger outgoing connections to the recorded network, while blues indicate the stimulated network has stronger incoming connections from the recorded network. Color code for functional assignments defined in Fig. 1B. Results are shown for 5 mice.

Figure 5B reveals a complex pattern of asymmetry, sometimes involving subregions of nominally homogeneous functionality, for example, subregions S1B and S1H of somatosensory cortex, and between somatosensory networks and parietal cortices.

Thy1-EC Matches Axonal Projection Connectivity More Closely than RS-FC

The higher spatial specificity of the Thy1-EC maps suggests that they could be reporting circuitry different from that reported by RS-FC analysis. To compare Thy1-EC maps to ex-vivo tracer studies, maps of axonal projection connectivity (APC) were collected from the Allen Mouse Brain Connectivity (AMBC) Atlas. The APC maps were spatially co-registered with the OIS data and stimulation sites closest to tracer injection sites (marked by "X" in Fig. 3B) were identified (Fig. 6). Because functional connectivity necessarily requires structural connectivity, in accordance with other rodent and primate studies, we do see similarities between RS-FC maps and regional APC. Although there is not a one-to-one correspondence between the labeled cells of the unbiased, pan-neuronal vector and the cells expressing Thy1. The strongest similarity between Thy1-EC and the APC data was observed within motor and sensory areas, the same 2 regions where there is strong asymmetry and reduced homotopic EC. These same regions overlapped most weakly with the RS-FC maps. When M2 is seeded, the RS-FC patterns show high connectivity to regions completely outside of the of tract boundaries within the APC images (Fig. 6, M2, RS-FC vs. Axonal Projection). The APC maps generally resembled Thy1-EC maps more than RS-FC maps. To calculate the spatial overlap between Thy1-EC or RS-FC and the APC maps, APC images were thresholded at 50% max intensity. The threshold for the Thy1-EC and RS-FC was chosen to be $z(r) = 0.3$, the median of all positive correlation coefficients in both sets of maps. For most sites evaluated, the spatial overlap (as determined by Dice coefficient) was higher between the Thy1-EC and APC maps, as compared to the RS-FC and APC maps (Fig. 6). The largest disparity was observed in M2 where the RS-FC patterns overlapped very little (Dice coefficient = 0.13) with the underlying APC maps, while the individual constellations of APC were nearly recapitulated in the Thy1-EC data (Dice = 0.50). Conversely, in M1, while both maps overlapped appreciably with the APC map, the RS-FC map resembled more closely the APC map (Dice = 0.65) compared with Thy1-EC (Dice = 0.52). As with any thresholding strategy, map overlap between the methods depends on the choice of cutoff. We evaluated a range of thresholds for the correlation coefficients ($z(r)$ from 0 to 1 in steps of 0.1) and intensity (0–100% in steps of 10%) and found that the overlap between Thy1-EC and APC was higher than RS-FC and APC in 63% of all thresholds applied (Fig. S10).

Axonal projection connectivity was evaluated at the 190 stimulation sites (Fig. 7A) for all 8 AMBC images. Regional APC was estimated by averaging the fluorescence intensity information within a 0.25 mm radius around each site (Fig. 7B, Axonal Projection Connectivity). APC generally was more similar to group-averaged Thy1-EC as compared to group-averaged RS-FC (Fig. 7B). Mean spatial similarity across all 3 types of connectivity was evaluated over all pixel pairs. This comparison yielded overall similarity measures as follows: corr(RS-FC,APC) < corr (Thy1-EC,APC) < corr(Thy1-EC,RS-FC) (Fig. 7C).

Discussion

Opto-EC mapping utilizes optogenetic mice to map local functional circuits based on the isolated excitation of specific neuronal populations throughout the cortex. We used Thy1-ChR2 transgenic mice and optical intrinsic signal imaging (OIS) to map effective connectivity (EC) patterns of Thy1-based circuits

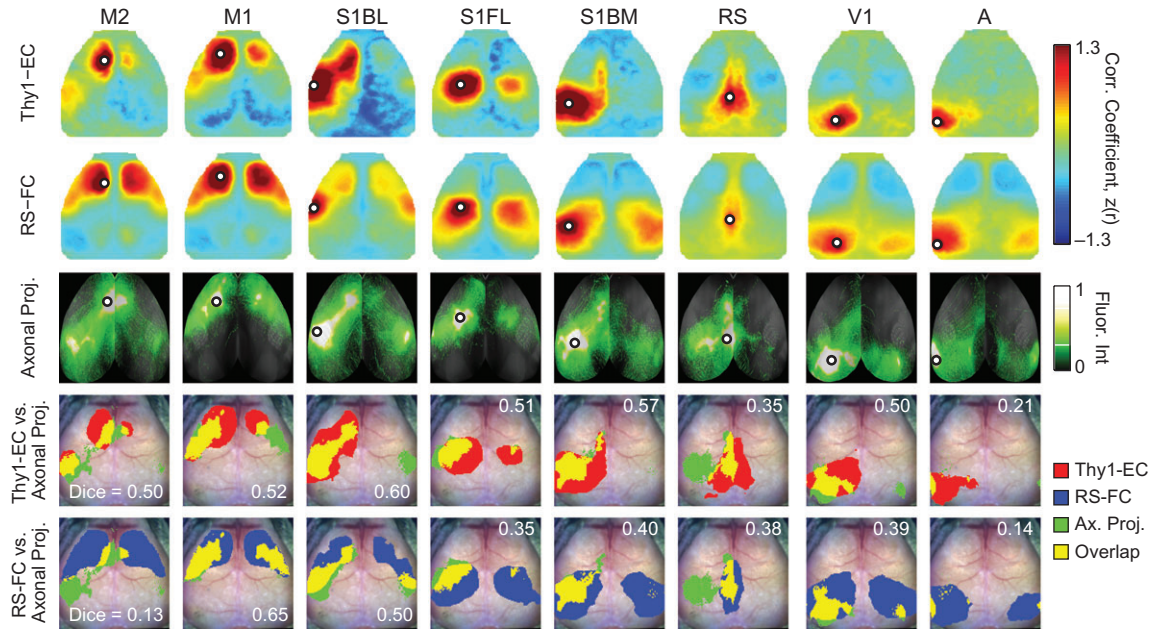

Figure 6. Maps of Thy1-EC more closely resemble cortical axonal projections compared to RS-FC maps. Maps of Thy1-EC and RS-FC are compared to axonal projection connectivity (APC) images for sites indicated by the "X" in Fig 3B. APC maps were collected from the Allen Mouse Brian Connectivity Atlas using the source search feature within the Mouse Connectivity Data Portal and projected onto the cortical surface using the cortical map signal viewer. APC images were co-registered to OIS imaging data and normalized by maximum fluorescence intensity. In order to calculate the spatial overlap between maps, Dice coefficients were calculated for Thy1-EC and RS-FC maps thresholded at $z(r) = 0.3$ and APC images thresholded at 0.5 after each image was normalized to its maximum intensity. In general, Thy1-EC maps were found to be more topographically similar to APC images than RS-FC maps. Maps of Thy1-EC and RS-FC are the same maps as shown in Fig. 3.

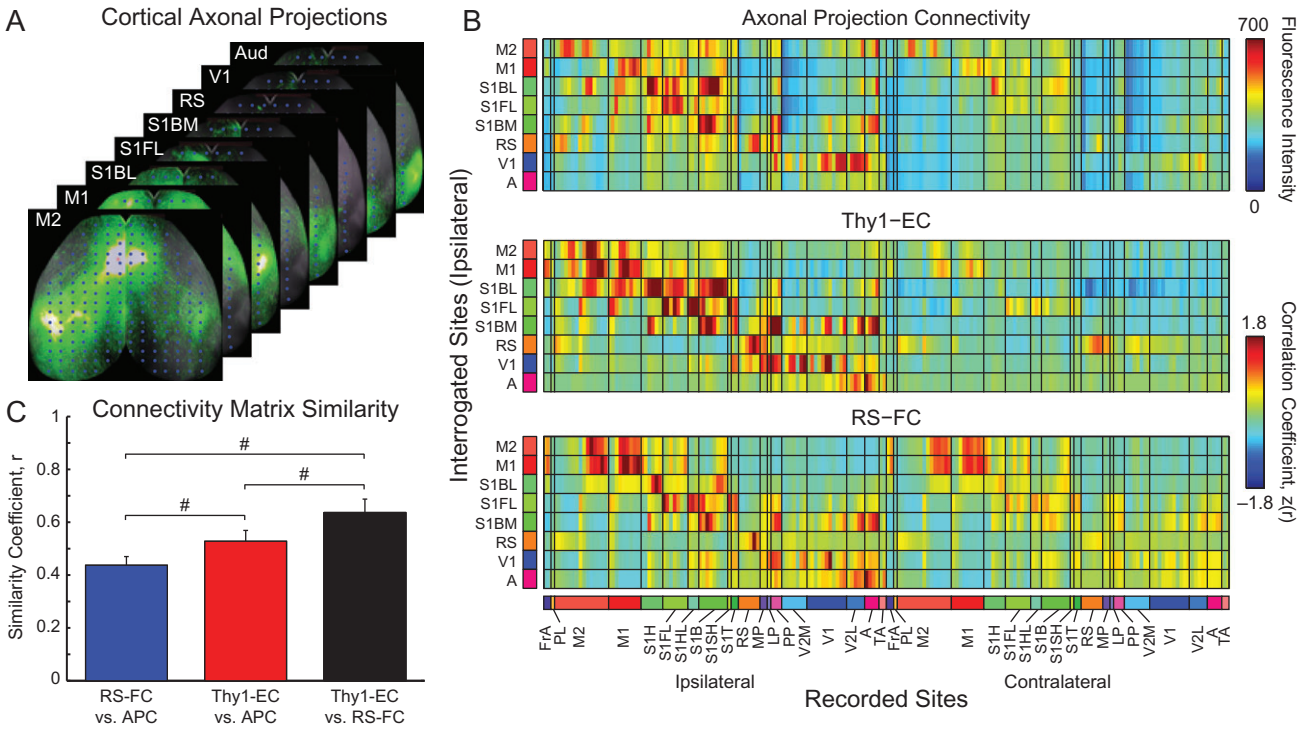

Figure 7. Thy1-EC provides intermediate connectivity information between axonal projection connectivity mapping and RS-FC mapping. (*A*) Site-wise connectivity from each of the 190 recording sites were gathered from 8 surface projection cortical maps from the Allen mouse Brain Connectivity Atlas for sites closest to those photostimulated. (*B*) Site-wise connectivity matrices for axonal projection connectivity (APC), Thy1-EC, and RS-FC modalities. Thy1-EC and RS-FC matrices report group-averaged results, color-coded by functional region. Rows represent interrogated sites (8 total) and columns represent the 190 recording sites over the cortex in 5 mice. Color code for functional assignments defined in Fig. 1B. (*C*) Similarity coefficients were calculated across matrices for each mouse, for each combination (RS-FC and APC, Thy1-EC and APC, and Thy1-EC and RS-FC). Bars represent mean ± standard deviation; $^{\#}P < 10^{-6}$.

(Thy1-EC) and RS-FC patterns of intrinsic brain activity. Our results suggest that, in awake mice, the connectivity structure of excitatory circuits revealed by Thy1-EC mapping lies in between axonal projection mapping and RS-FC mapping. Compared to ex-vivo techniques, the more general method of Opto-EC mapping can be performed in individual awake, sleeping, or anesthetized animals and does not require craniotomies or multiple viral injections for transfecting multiple brain sites. We mapped Opto-EC at 100 stimulation sites in less than an hour. Thus, this technique represents a highly efficient strategy for examining structure–function relationships and, potentially, evolving connectivity-related circuit plasticity.

ChR2-evoked Hemodynamic Signals

The goal of evaluating different stimulus parameters was to find photostimuli that produced short ChR2-HRs with single pulse trains and high CNR to facilitate rapid mapping of Thy1-based cortical nodes. Stimulation of other cell-types, (e.g., inhibitory neurons) might require a different optimized set of photostimuli (Anenberg et al. 2015). While candidate responses were found following several stimulus combinations, we chose to map Thy1-based circuits over the cortex using 10 Hz, 3 s pulse trains. Stimuli with increased optical power might also yield useable mapping responses, but changes in cerebral blood flow (Rungta et al. 2017) or negative BOLD responses (Christie et al. 2013) have been reported in naive animals using power densities higher than those used here. Accordingly, we did not investigate laser power greater than 0.5 mW or pulse widths greater than 5 ms (maximum duty cycle investigated was 10%).

Fast Versus Slow Hemodynamic Responses

Optogenetically evoked hemodynamic responses very closely resemble responses to peripheral stimulation (Desai et al. 2011; Kahn et al. 2011; Scott and Murphy 2012; Vazquez et al. 2014; Iordanova et al. 2015), and sum in an approximately linear manner with measures of local neural activity (Kahn et al. 2011; Ji et al. 2012). Further, both types of stimuli can elicit fast and slow components. Fast responses can be largely invariant across a wide range of short-duration stimuli (5–2000 ms) (Devor et al. 2003; Martindale et al. 2003; Culver et al. 2005; Berwick et al. 2008; Hirano et al. 2011), while the temporal characteristics of the slow response are more variable. Some groups observe a peak/plateau response to long-duration stimuli (10 s or greater) where the plateau is lower in magnitude than the initial peak (Dunn et al. 2005; Martindale et al. 2005). Others observe a slow response greater than the initial peak or continued rise throughout the course of stimulation (Boynton et al. 1996; Mandeville et al. 1999; Logothetis et al. 2001; Culver et al. 2005; Lee et al. 2010; Iordanova et al. 2015). The magnitude of the slow responses of HbR in Figure 2, and many in Figure S2, appear to be more constant than the slow responses of HbO and HbT (though, in all cases, the area under the curve increases with increasing stimulus duration). This result is not entirely unexpected, as others have also reported constant HbR-weighted responses to photostimulus trains of varying

durations (Culver et al. 2005; Desai et al. 2011) (also see Ji et al. 2012).

It has been suggested (Pfeuffer et al. 2003) that the early onset responses following stimulation originate in gray matter, while longer latency responses are of vascular origin. The role of the vasculature itself as part of the neurovascular coupling chain is becoming increasingly emphasized. Mandeville and colleagues (Mandeville et al. 1999) have suggested that the ratio of peak-to-plateau in responses to long-duration peripheral stimuli is greater in arteries than in either parenchyma or veins, so capillaries versus larger vessels could play different roles in the temporal dynamics of the measured responses. Selective interruption of endothelial signaling has been shown to block retrograde dilation of pial arteries and subsequent hemodynamic responses (Chen et al. 2014). Endothelial signaling also contains both fast and slow components (Hillman 2014) that could partially account for the fast and slow components of the hemodynamic responses.

Differences Between RS-FC and Thy1-EC Patterns

"Resting state" is an operational definition referring to a paradigm in which intrinsic activity is recorded in the absence of imposed environmental stimuli (or overt motor behaviors); this condition can only be approximated experimentally. Potential stimuli in the quiet environment of the imaging room include the imaging LEDs (although the eyes are covered to prevent direct visual stimulation), cooling fans, and other ambient room noise. This condition is analogous to "resting-state" paradigms in human fMRI where subjects are asked to lay in the imaging system, but able to hear the noise from the scanner and feel the bore. Importantly, these noise sources are constant; that is, free of detectable events (discounting what cannot be controlled in the environment). Although ambient noise might exert a small modulatory role in shaping ongoing intrinsic activity, its contribution to patterns of RS-FC are minimal compared to modulations of brain activity due to discrete stimuli, for example, as in event-related or task-based paradigms. The similarity between the awake RS-FC maps and those from our previously published studies in mice under ketamine anesthesia (White et al. 2011; Bauer et al. 2014; Bumstead et al. 2016) supports the idea that the animals are indeed in a comparable state of rest while awake in our imaging system.

Differences between RS-FC and Thy1-EC patterns likely are not due to the neurovascular response properties of the brain. In general, OIS and BOLD measures are most highly correlated with local field potentials (LFPs), although multi-unit activity (MUA) can account for a non-negligible fraction of the variance in hemodynamic signaling. Because of the tight coupling between MUA and LFPs at rest (Shmuel and Leopold 2008) and in task responses (Sanganahalli et al. 2009), analyses of spontaneous BOLD fluctuations in relation to underlying LFPs and MUA have found similar agreement to analyses of stimulus-evoked BOLD fluctuations (Logothetis et al. 2001). These results suggest that neurovascular coupling associated with dynamic neural fluctuations and OIS (or BOLD) variance is similar for resting state and task-based measures (Hyder and Rothman 2010).

One major difference between Thy1-EC and RS-FC patterns is the degree to which homotopic regions share coordinated activity. Bilateral symmetry of RS-FC maps is very well documented in multiple species on the basis of fMRI and optical techniques (Vincent et al. 2007; Shehzad et al. 2009; Mohajerani et al. 2010; White et al. 2011; Eggebrecht et al. 2014). Synchronous activity between homotopic cortical regions reflected in RS-FC maps may reflect direct monosynaptic callosal connections or polysynaptic circuits including subcortical structures. RS-FC in the visual cortex of monkeys most likely involves polysynaptic pathways (Vincent et al. 2007), and indirect cortico-cortical structural connections predict interhemispheric RS-FC between visual cortices in humans (Honey et al. 2009). Deep nuclei can also regulate cortical excitation/inhibition (Porter and Nieves 2004; Poulet et al. 2012; Taub et al. 2013), and may do so selectively (for example, so that homotopic regions are excitable at the same time (Xiao et al. 2017)).

In contrast, cortical homotopic contralateral Thy1-EC is highly variable. The diverse set of projections of Thy1-based cortical neurons might contribute to the wide range of homotopic Thy1-EC values observed here. Responses to photostimulation of ChR2-expressing Thy1 neurons could reflect direct (monosynaptic) excitation via transcallosal projections (Koralek and Killackey 1990; Hattox and Nelson 2007) (e.g., S1fp, S1hp) or indirect (multisynaptic) excitation of cortico-cortico (Petreanu et al. 2007; Weiler et al. 2008; Vazquez et al. 2014), cortico-striatal (Donoghue and Kitai 1981; Cowan and Wilson 1994), and cortico-thalamic circuits (Veinante et al. 2000; Hattox and Nelson 2007; Mao et al. 2011). Whole-brain mapping of optogenetically defined connections in rodents potentially could determine which cell populations support patterns of spontaneous brain activity. For example, mirrored, bilateral motor responses are observed when anterior, but not posterior, CaMKIIα-expressing excitatory neurons of the thalamus are photostimulated (Lee et al. 2010). This circuit could, in part, drive bilaterally synchronized intrinsic activity in motor cortex. In the context of examining disease models, many brain disorders result in disruption of homotopic RS-FC (van Meer et al. 2010; Zhang and Raichle 2010; Bero et al. 2012; Carter et al. 2012; Bauer et al. 2014). Mapping the causal connectivity between optogenetically defined subcomponents of RSNs might be particularly useful for examining circuit dysfunction during disease progression.

Anticorrelations in Thy1-EC and RS-FC Maps

We observed anticorrelations to varying degrees in the present Thy1-EC as well as RS-FC results, a finding entirely consistent with prior RS-FC studies by us (White et al. 2011; Bauer et al. 2014) and others (Fox et al. 2009). These anticorrelations appear in many of the same brain regions (anticorrelations between anterior and posterior brain regions) across methods (Thy1-EC and RS-FC), although some differences do exist. Interpreting anticorrelations in neuroimaging data is complicated by a common preprocessing step when calculating measurements of functional connectivity. Shared variance across the brain can obscure measurements of regional functional connectivity (e.g., using zero-lag correlation analysis as performed in this study). One frequently used preprocessing step to increase the spatial specificity of functional connectivity patterns is the regression of a whole brain or "global" signal prior to correlation analysis. A consequence of global signal regression is that the distribution of correlation coefficients over the brain becomes approximately zero-centered (relevant algebra is given in the supplemental of Fox et al. (2009)). Experiments specifically designed to further our understanding of the neurophysiology of anticorrelations in either RS-FC or Thy1-EC maps could be conducted in mice by combining optical imaging with electrical recordings of LFPs (Lu et al. 2007; He et al. 2008).

Asymmetry in Thy1-EC maps

In the rodent, whisker-based tactile sensation and sensorimotor integration are mediated in part by a connection loop between somatosensory barrel and motor cortices (Ferezou et al. 2007). The existence of reciprocal connectivity strengths at the level of the cortex provides an opportunity for validating the sensitivity of hemodynamic-based assessments of directionality. Previous reports have also shown directionality within this system using anatomical tracers (Ferezou et al. 2007; Hattox and Nelson 2007; Sato and Svoboda 2010) and other local (Petreanu et al. 2007; Mao et al. 2011) and global (Ayling et al. 2009; Lim et al. 2012) ChR2-based methods. Thus, hemodynamic measures of Thy1-EC within these regions appear to reflect the known input-output organization of mouse motor and somatosensory cortices.

Asymmetric anatomical connectivity between cortical regions outside the somatomotor systems has been less well studied. We observed Thy1-EC asymmetry between somatosensory regions and parietal association regions (Fig. 5*B*). Parietal cortex is widely regarded as a hub for integrating multisensory information in the mouse (Kolb and Walkey 1987; Lim et al. 2012, 2015). It has been reported that sensory stimulation and photostimulation both induce propagated activity that terminates at a common sink in parietal association areas (Mohajerani et al. 2013). These potential functional relationships may generate asymmetries in Opto-EC measures. Additional work is needed to study how Opto-EC asymmetries relate to large-scale cortical processing in the mouse (Kamatani et al. 2007).

Thy1-EC Resides Between Structural Connectivity and Resting State Functional Connectivity Methods

APC mapping relies on viral gene transfer of EGFP into projecting neurons and permits the visualization of axonal projections originating from the site of injection. The similarity between Thy1-EC and APC suggests that Thy1-EC maps tend to reflect pair-wise connectivity between neurons, much like electrical stimulation of the cortex (Matsui et al. 2011; Keller et al. 2014). In contrast, RS-FC appears to largely reflect polysynaptic pathways. Certain complications attend these inferences. In particular, ChR2-evoked hemodynamic responses can occur without glutamatergic synaptic transmission (Scott and Murphy 2012). On the other hand, some excitatory, intracortical connectivity patterns do require multisynaptic communication as the application of glutamate blockers abolishes interhemispheric Thy1-EC (Lim et al. 2012). The current Thy1-EC paradigm yields results similar to APC mapping. It is unclear if different optogenetic stimulation parameters may permit a bias tilt towards more or less direct (polysynaptic) effective connectivity (see Fig. S9). On the basis of the similarity measures shown in Figure 7, we suggest that Opto-EC maps may serve as a bridge between RS-FC, which reflects intrinsic activity, and tracer mapping, which reflects anatomical connectivity.

Considerations and Future Directions

Compared to imaging methods directly related to electrophysiology, for example, calcium indicators (Vanni and Murphy 2014; Ma et al. 2016; Wright et al. 2017), and voltage sensitive dyes (Ferezou et al. 2007; Lim et al. 2012), the hemodynamic response is ~5–100× slower. However, this slowness does not compromise studies focused on topography as opposed to neural dynamics. Hemodynamic mapping with single pulse trains produces maps topographically similar to those obtained using voltage sensitive dyes (Ferezou et al. 2007; Lim et al. 2012, 2014). Mapping Opto-EC with OIS (or fMRI) does not require removing the skull, which is a significant advantage in longitudinal studies.

Our preliminary experiments indicated that stimulus trains were necessary to generate reliable ChR2-HRs. Future studies might examine whether useful CNR can be obtained with single pulses. Previous studies suggest that broader ipsilateral network activity can be obtained by increasing the pulse duration of the optogenetic stimulus (Vazquez et al. 2014; Iordanova et al. 2015). Although we have not exhaustively explored stimulus frequencies and pulse train durations, we did observe that homotopic Thy1-EC in forepaw somatosensory cortex modestly depended on photostimulus frequency (Fig. S9). Thus, it is possible that different stimulus protocols might reveal intricacies of network communication not otherwise revealed by traditional task or resting state-based imaging paradigms.

The transgenic mice used for Thy1-EC mapping primarily express ChR2 within layer 5 pyramidal neurons, but other minority cell populations throughout the cortex as well as axons of passage might also express ChR2 (Petreanu et al. 2007; Wang et al. 2007). Given the relatively low laser power delivered to the tissue surface, and the large extinction coefficient of blue light in biological tissue (Prahl 2002), Thy1-EC patterns primarily result from stimulation of superficial dendritic processes of deeper layer 5 neurons and downstream (orthodromic) synaptic targets. As with other planar imaging methods, connectivity information between stimulated cortical sites and deeper brain structures (e.g., thalamus) cannot be determined, and will require whole-brain mapping with fMRI or other tomographic approaches (Bauer et al. 2011; Eggebrecht et al. 2014; Nasiriavanaki et al. 2014; Reisman et al. 2017). Previous studies in rodents demonstrating optogenetically defined connectivity using fMRI (Lee et al. 2010; Desai et al. 2011) were limited to stimulating single sites and required craniotomies for implanting fiber optics (Desai et al. 2011). Further, those studies used viral vectors to target specific neural subtypes (Lee et al. 2010; Desai et al. 2011) which precludes whole-brain mapping experiments without multiple invasive injections. While recent technological advances have enabled reliable RS-FC mapping in the mouse brain (Stafford et al. 2014; Liska et al. 2015; Bergmann et al. 2016), space constraints within the bore have so far prevented relating global Opto-EC mapping to RS-FC in the mouse. Given that Opto-EC mapping method can be extended to fMRI, perhaps fiber-optic or other solutions will soon be discovered that allow for more thorough examinations of how optogenetically defined effective connectivity patterns contribute to RSNs in the mouse.

Conclusion

Results of this study suggest that Opto-EC mapping provides complementary information to RS-FC mapping regarding the functional organization of the brain. Extension of optical stimulation methods to fMRI could allow for more thorough examinations of how structural connectivity contributes to RS-FC or how patterns of RS-FC arise from intrinsic activity within different populations of cells. Further, the ability to map effective connectivity in the brains of individual mice in seconds allows for longitudinal imaging experiments. By providing an assay that bridges between ex-vivo retrograde tracer labeling and RS-FC, Opto-EC could be particularly useful for understanding the

relationship between structural and functional connectivity or for longitudinal investigation of changing or plastic functional organization within the brain.

Supplementary Material

Supplementary data are available at *Cerebral Cortex* online.

Notes

This work was supported in part by National Institutes of Health grants K25NS083754 (AQB), R01NS078223 (JPC), R01NS084028 (J-ML), P30NS098577 (AZS), and American Heart Association grant 14PRE18410013 (AWK). *Conflict of Interest*: None declared.

References

Alivisatos AP, Andrews AM, Boyden ES, Chun M, Church GM, Deisseroth K, Donoghue JP, Fraser SE, Lippincott-Schwartz J, Looger LL, et al. 2013. Nanotools for neuroscience and brain activity mapping. ACS Nano. 7:1850–1866.

Anenberg E, Chan AW, Xie Y, LeDue JM, Murphy TH. 2015. Optogenetic stimulation of GABA neurons can decrease local neuronal activity while increasing cortical blood flow. J Cereb Blood Flow Metab. 35:1579–1586.

Arridge SR, Cope M, Delpy DT. 1992. The theoretical basis for the determination of optical pathlengths in tissue: temporal and frequency analysis. Phys Med Biol. 37:1531–1560.

Ayling OG, Harrison TC, Boyd JD, Goroshkov A, Murphy TH. 2009. Automated light-based mapping of motor cortex by photoactivation of channelrhodopsin-2 transgenic mice. Nat Methods. 6:219–224.

Bauer AQ, Kraft AW, Wright PW, Snyder AZ, Lee JM, Culver JP. 2014. Optical imaging of disrupted functional connectivity following ischemic stroke in mice. Neuroimage. 99:388–401.

Bauer AQ, Nothdurft RE, Erpelding TN, Wang LV, Culver JP. 2011. Quantitative photoacoustic imaging: correcting for heterogeneous light fluence distributions using diffuse optical tomography. J Biomed Opt. 16:096016.

Beckmann CF, DeLuca M, Devlin JT, Smith SM. 2005. Investigations into resting-state connectivity using independent component analysis. Philos Trans R Soc Lond B Biol Sci. 360:1001–1013.

Bergmann E, Zur G, Bershadsky G, Kahn I. 2016. The organization of mouse and human cortico-hippocampal networks estimated by intrinsic functional connectivity. Cereb Cortex. 26(12):4497–4512.

Bero AW, Bauer AQ, Stewart FR, White BR, Cirrito JR, Raichle ME, Culver JP, Holtzman DM. 2012. Bidirectional relationship between functional connectivity and amyloid-beta deposition in mouse brain. J Neurosci. 32:4334–4340.

Berwick J, Johnston D, Jones M, Martindale J, Martin C, Kennerley AJ, Redgrave P, Mayhew JEW. 2008. Fine detail of neurovascular coupling revealed by spatiotemporal analysis of the hemodynamic response to single whisker stimulation in rat barrel cortex. J Neurophysiol. 99:787–798.

Biswal B, Yetkin FZ, Haughton VM, Hyde JS. 1995. Functional connectivity in the motor cortex of resting human brain using echo-planar MRI. Magn Reson Med. 34:537–541.

Biswal BB, Mennes M, Zuo XN, Gohel S, Kelly C, Smith SM, Beckmann CF, Adelstein JS, Buckner RL, Colcombe S, et al. 2010. Toward discovery science of human brain function. Proc Natl Acad Sci USA. 107:4734–4739.

Bouchard MB, Chen BR, Burgess SA, Hillman EM. 2009. Ultrafast multispectral optical imaging of cortical oxygenation, blood flow, and intracellular calcium dynamics. Opt Express. 17:15670–15678.

Boyden ES, Zhang F, Bamberg E, Nagel G, Deisseroth K. 2005. Millisecond-timescale, genetically targeted optical control of neural activity. Nat Neurosci. 8:1263–1268.

Boynton GM, Engel SA, Glover GH, Heeger DJ. 1996. Linear systems analysis of functional magnetic resonance imaging in human V1. J Neurosci. 16:4207–4221.

Bumstead JR, Bauer AQ, Wright PW, Culver JP. 2016. Cerebral functional connectivity and Mayer waves in mice: phenomena and separability. J Cereb Blood Flow Metab. 37(2):471–484.

Carter AR, Patel KR, Astafiev SV, Snyder AZ, Rengachary J, Strube MJ, Pope A, Shimony JS, Lang CE, Shulman GL, et al. 2012. Upstream dysfunction of somatomotor functional connectivity after corticospinal damage in stroke. Neurorehabil Neural Repair. 26:7–19.

Chen BR, Kozberg MG, Bouchard MB, Shaik MA, Hillman EM. 2014. A critical role for the vascular endothelium in functional neurovascular coupling in the brain. J Am Heart Assoc. 3:e000787.

Chernov MM, Chen G, Torre-Healy LA, Friedman RM, Roe AW. 2016. Microelectrode array stimulation combined with intrinsic optical imaging: a novel tool for functional brain mapping. J Neurosci Methods. 263:7–14.

Christie IN, Wells JA, Southern P, Marina N, Kasparov S, Gourine AV, Lythgoe MF. 2013. fMRI response to blue light delivery in the naïve brain: implications for combined optogenetic fMRI studies. Neuroimage. 66:634–641.

Cowan RL, Wilson CJ. 1994. Spontaneous firing patterns and axonal projections of single corticostriatal neurons in the rat medial agranular cortex. J Neurophysiol. 71:17–32.

Culver JP, Siegel AM, Franceschini MA, Mandeville JB, Boas DA. 2005. Evidence that cerebral blood volume can provide brain activation maps with better spatial resolution than deoxygenated hemoglobin. Neuroimage. 27:947–959.

Damoiseaux JS, Greicius MD. 2009. Greater than the sum of its parts: a review of studies combining structural connectivity and resting-state functional connectivity. Brain Struct Funct. 213:525–533.

Damoiseaux JS, Rombouts SA, Barkhof F, Scheltens P, Stam CJ, Smith SM, Beckmann CF. 2006. Consistent resting-state networks across healthy subjects. Proc Natl Acad Sci USA. 103:13848–13853.

Desai M, Kahn I, Knoblich U, Bernstein J, Atallah H, Yang A, Kopell N, Buckner RL, Graybiel AM, Moore CI, et al. 2011. Mapping brain networks in awake mice using combined optical neural control and fMRI. J Neurophysiol. 105:1393–1405.

Devor A, Dunn AK, Andermann ML, Ulbert I, Boas DA, Dale AM. 2003. Coupling of total hemoglobin concentration, oxygenation, and neural activity in rat somatosensory cortex. Neuron. 39:353–359.

Dombeck DA, Harvey CD, Tian L, Looger LL, Tank DW. 2010. Functional imaging of hippocampal place cells at cellular resolution during virtual navigation. Nat Neurosci. 13:1433–1440.

Donoghue JP, Kitai ST. 1981. A collateral pathway to the neostriatum from corticofugal neurons of the rat sensory-motor cortex: an intracellular HRP study. J Comp Neurol. 201:1–13.

Dowling JL, Henegar MM, Liu D, Rovainen CM, Woolsey TA. 1996. Rapid optical imaging of whisker responses in the rat barrel cortex. J Neurosci Methods. 66:113–122.

Dunn AK, Devor A, Dale AM, Boas DA. 2005. Spatial extent of oxygen metabolism and hemodynamic changes during functional activation of the rat somatosensory cortex. Neuroimage. 27:279–290.

Eggebrecht AT, Ferradal SL, Robichaux-Viehoever A, Hassanpour MS, Dehghani H, Snyder AZ, Hershey T, Culver JP. 2014. Mapping distributed brain function and networks with diffuse optical tomography. Nat Photonics. 8:448–454.

Entz L, Tóth E, Keller CJ, Bickel S, Groppe DM, Fabó D, Kozák LR, Erőss L, Ulbert I, Mehta AD. 2014. Evoked effective connectivity of the human neocortex. Hum Brain Mapp. 35: 5736–5753.

Ferezou I, Haiss F, Gentet LJ, Aronoff R, Weber B, Petersen CCH. 2007. Spatiotemporal dynamics of cortical sensorimotor integration in behaving mice. Neuron. 56:907–923.

Ferradal SL, Liao SM, Eggebrecht AT, Shimony JS, Inder TE, Culver JP, Smyser CD. 2016. Functional imaging of the developing brain at the bedside using diffuse optical tomography. Cereb Cortex. 26:1558–1568.

Fornito A, Zalesky A, Breakspear M. 2015. The connectomics of brain disorders. Nat Rev Neurosci. 16:159–172.

Fox MD, Zhang D, Snyder AZ, Raichle ME. 2009. The global signal and observed anticorrelated resting state brain networks. J Neurophysiol. 101:3270–3283.

Friston K, Moran R, Seth AK. 2013. Analysing connectivity with Granger causality and dynamic causal modelling. Curr Opin Neurobiol. 23:172–178.

Friston KJ. 2011. Functional and effective connectivity: a review. Brain Connect. 1:13–36.

Friston KJ, Frith CD, Frackowiak RSJ. 1993. Time-dependent changes in effective connectivity measured with PET. Hum Brain Mapp. 1:69–79.

Frostig RD, Lieke EE, Ts'o DY, Grinvald A. 1990. Cortical functional architecture and local coupling between neuronal activity and the microcirculation revealed by in vivo high-resolution optical imaging of intrinsic signals. Proc Natl Acad Sci USA. 87:6082–6086.

Gibson JR, Beierlein M, Connors BW. 1999. Two networks of electrically coupled inhibitory neurons in neocortex. Nature. 402:75–79.

Grinvald A, Lieke E, Frostig RD, Gilbert CD, Wiesel TN. 1986. Functional architecture of cortex revealed by optical imaging of intrinsic signals. Nature. 324:361–364.

Hattox AM, Nelson SB. 2007. Layer V neurons in mouse cortex projecting to different targets have distinct physiological properties. J Neurophysiol. 98:3330–3340.

He BJ, Snyder AZ, Zempel JM, Smyth MD, Raichle ME. 2008. Electrophysiological correlates of the brain's intrinsic large-scale functional architecture. Proc Natl Acad Sci USA. 105: 16039–16044.

Hillman EMC. 2014. Coupling mechanism and significance of the BOLD signal: a status report. Annu Rev Neurosci. 37: 161–181.

Hirano Y, Stefanovic B, Silva AC. 2011. Spatiotemporal evolution of the functional magnetic resonance imaging response to ultrashort stimuli. J Neurosci. 31:1440–1447.

Histed MH, Bonin V, Reid RC. 2009. Direct activation of sparse, distributed populations of cortical neurons by electrical microstimulation. Neuron. 63:508–522.

Honey CJ, Sporns O, Cammoun L, Gigandet X, Thiran JP, Meuli R, Hagmann P. 2009. Predicting human resting-state functional connectivity from structural connectivity. Proc Natl Acad Sci USA. 106:2035–2040.

Honey CJ, Thivierge JP, Sporns O. 2010. Can structure predict function in the human brain? Neuroimage. 52:766–776.

Hyder F, Rothman DL. 2010. Neuronal correlate of BOLD signal fluctuations at rest: err on the side of the baseline. Proc Natl Acad Sci USA. 107:10773–10774.

Iordanova B, Vazquez AL, Poplawsky AJ, Fukuda M, Kim SG. 2015. Neural and hemodynamic responses to optogenetic and sensory stimulation in the rat somatosensory cortex. J Cereb Blood Flow Metab. 35:922–932.

Ji L, Zhou J, Zafar R, Kantorovich S, Jiang R, Carney PR, Jiang H. 2012. Cortical neurovascular coupling driven by stimulation of channelrhodopsin-2. PLoS One. 7:e46607.

Jones EG. 1999. Making brain connections: neuroanatomy and the work of TPS Powell, 1923–1996. Annu Rev Neurosci. 22: 49–103.

Kahn I, Desai M, Knoblich U, Bernstein J, Henninger M, Graybiel AM, Boyden ES, Buckner RL, Moore CI. 2011. Characterization of the functional MRI response temporal linearity via optical control of neocortical pyramidal neurons. J Neurosci. 31: 15086–15091.

Kamatani D, Hishida R, Kudoh M, Shibuki K. 2007. Experience-dependent formation of activity propagation patterns at the somatosensory S1 and S2 boundary in rat cortical slices. Neuroimage. 35:47–57.

Keller CJ, Honey CJ, Entz L, Bickel S, Groppe DM, Toth E, Ulbert I, Lado FA, Mehta AD. 2014. Corticocortical evoked potentials reveal projectors and integrators in human brain networks. J Neurosci. 34:9152–9163.

Kolb B, Walkey J. 1987. Behavioural and anatomical studies of the posterior parietal cortex in the rat. Behav Brain Res. 23: 127–145.

Koralek KA, Killackey HP. 1990. Callosal projections in rat somatosensory cortex are altered by early removal of afferent input. Proc Natl Acad Sci USA. 87:1396–1400.

Lee JH, Durand R, Gradinaru V, Zhang F, Goshen I, Kim DS, Fenno LE, Ramakrishnan C, Deisseroth K. 2010. Global and local fMRI signals driven by neurons defined optogenetically by type and wiring. Nature. 465:788–792.

Lein ES, Hawrylycz MJ, Ao N, Ayres M, Bensinger A, Bernard A, Boe AF, Boguski MS, Brockway KS, Byrnes EJ, et al. 2007. Genome-wide atlas of gene expression in the adult mouse brain. Nature. 445:168–176.

Liao SM, Ferradal SL, White BR, Gregg N, Inder TE, Culver JP. 2012. High-density diffuse optical tomography of term infant visual cortex in the nursery. J Biomed Opt. 17:081414.

Lim DH, LeDue JM, Mohajerani MH, Murphy TH. 2014. Optogenetic mapping after stroke reveals network-wide scaling of functional connections and heterogeneous recovery of the peri-infarct. J Neurosci. 34:16455–16466.

Lim DH, LeDue JM, Murphy TH. 2015. Network analysis of mesoscale optical recordings to assess regional, functional connectivity. Neurophotonics. 2:041405.

Lim DH, Mohajerani MH, Ledue J, Boyd J, Chen S, Murphy TH. 2012. In vivo large-scale cortical mapping using channelrhodopsin-2 stimulation in transgenic mice reveals asymmetric and reciprocal relationships between cortical areas. Front Neural Circuits. 6:11.

Liska A, Galbusera A, Schwarz AJ, Gozzi A. 2015. Functional connectivity hubs of the mouse brain. Neuroimage. 115: 281–291.

Logothetis NK, Pauls J, Augath M, Trinath T, Oeltermann A. 2001. Neurophysiological investigation of the basis of the fMRI signal. Nature. 412:150–157.

Lu H, Zuo Y, Gu H, Waltz JA, Zhan W, Scholl CA, Rea W, Yang Y, Stein EA. 2007. Synchronized delta oscillations correlate with the resting-state functional MRI signal. Proc Natl Acad Sci USA. 104:18265–18269.

Ma Y, Shaik MA, Kozberg MG, Kim SH, Portes JP, Timerman D, Hillman EM. 2016. Resting-state hemodynamics are spatiotemporally coupled to synchronized and symmetric neural activity in excitatory neurons. Proc Natl Acad Sci USA. 113: E8463–E8471.

Mandeville JB, Marota JJ, Ayata C, Zaharchuk G, Moskowitz MA, Rosen BR, Weisskoff RM. 1999. Evidence of a cerebrovascular postarteriole windkessel with delayed compliance. J Cereb Blood Flow Metab. 19:679–689.

Mao T, Kusefoglu D, Hooks BM, Huber D, Petreanu L, Svoboda K. 2011. Long-range neuronal circuits underlying the interaction between sensory and motor cortex. Neuron. 72:111–123.

Martindale J, Berwick J, Martin C, Kong Y, Zheng Y, Mayhew J. 2005. Long duration stimuli and nonlinearities in the neural-haemodynamic coupling. J Cereb Blood Flow Metab. 25:651–661.

Martindale J, Mayhew J, Berwick J, Jones M, Martin C, Johnston D, Redgrave P, Zheng Y. 2003. The hemodynamic impulse response to a single neural event. J Cereb Blood Flow Metab. 23:546–555.

Massimini M, Ferrarelli F, Huber R, Esser SK, Singh H, Tononi G. 2005. Breakdown of cortical effective connectivity during sleep. Science. 309:2228–2232.

Matsui T, Koyano KW, Tamura K, Osada T, Adachi Y, Miyamoto K, Chikazoe J, Kamigaki T, Miyashita Y. 2012. FMRI activity in the macaque cerebellum evoked by intracortical microstimulation of the primary somatosensory cortex: evidence for polysynaptic propagation. PLoS One. 7:e47515.

Matsui T, Tamura K, Koyano KW, Takeuchi D, Adachi Y, Osada T, Miyashita Y. 2011. Direct comparison of spontaneous functional connectivity and effective connectivity measured by intracortical microstimulation: an fMRI study in macaque monkeys. Cereb Cortex. 21:2348–2356.

Matsumoto R, Nair DR, LaPresto E, Najm I, Bingaman W, Shibasaki H, Lüders HO. 2004. Functional connectivity in the human language system: a cortico-cortical evoked potential study. Brain. 127:2316–2330.

Mattis J, Tye KM, Ferenczi EA, Ramakrishnan C, O'Shea DJ, Prakash R, Gunaydin LA, Hyun M, Fenno LE, Gradinaru V, et al. 2011. Principles for applying optogenetic tools derived from direct comparative analysis of microbial opsins. Nat Methods. 9:159–172.

McCasland JS, Hibbard LS, Rhoades RW, Woolsey TA. 1997. Activation of a wide-spread network of inhibitory neurons in barrel cortex. Somatosens Mot Res. 14:138–147.

Mohajerani MH, Chan AW, Mohsenvand M, LeDue J, Liu R, McVea DA, Boyd JD, Wang YT, Reimers M, Murphy TH. 2013. Spontaneous cortical activity alternates between motifs defined by regional axonal projections. Nat Neurosci. 16: 1426–1435.

Mohajerani MH, McVea DA, Fingas M, Murphy TH. 2010. Mirrored bilateral slow-wave cortical activity within local circuits revealed by fast bihemispheric voltage-sensitive dye imaging in anesthetized and awake mice. J Neurosci. 30: 3745–3751.

Nasiriavanaki M, Xia J, Wan H, Bauer AQ, Culver JP, Wang LV. 2014. High-resolution photoacoustic tomography of resting-state functional connectivity in the mouse brain. Proc Natl Acad Sci USA. 111:21–26.

O'Reilly JX, Croxson PL, Jbabdi S, Sallet J, Noonan MP, Mars RB, Browning PG, Wilson CR, Mitchell AS, Miller KL, et al. 2013. Causal effect of disconnection lesions on interhemispheric functional connectivity in rhesus monkeys. Proc Natl Acad Sci USA. 110:13982–13987.

Oh SW, Harris JA, Ng L, Winslow B, Cain N, Mihalas S, Wang Q, Lau C, Kuan L, Henry AM, et al. 2014. A mesoscale connectome of the mouse brain. Nature. 508:207–214.

Otte WM, van der Marel K, van Meer MP, van Rijen PC, Gosselaar PH, Braun KP, Dijkhuizen RM. 2015. Altered contralateral sensorimotor system organization after experimental hemispherectomy: a structural and functional connectivity study. J Cereb Blood Flow Metab. 35:1358–1367.

Petkov CI, Kikuchi Y, Milne AE, Mishkin M, Rauschecker JP, Logothetis NK. 2015. Different forms of effective connectivity in primate frontotemporal pathways. Nat Commun. 6:6000.

Petreanu L, Huber D, Sobczyk A, Svoboda K. 2007. Channelrhodopsin-2-assisted circuit mapping of long-range callosal projections. Nat Neurosci. 10:663–668.

Pfeuffer J, McCullough JC, Van de Moortele PF, Ugurbil K, Hu X. 2003. Spatial dependence of the nonlinear BOLD response at short stimulus duration. Neuroimage. 18:990–1000.

Porter JT, Nieves D. 2004. Presynaptic GABAB receptors modulate thalamic excitation of inhibitory and excitatory neurons in the mouse barrel cortex. J Neurophysiol. 92:2762–2770.

Poulet JFA, Fernandez LMJ, Crochet S, Petersen CCH. 2012. Thalamic control of cortical states. Nat Neurosci. 15: 370–372.

Power JD, Cohen AL, Nelson SM, Wig GS, Barnes KA, Church JA, Vogel AC, Laumann TO, Miezin FM, Schlaggar BL, et al. 2011. Functional network organization of the human brain. Neuron. 72:665–678.

Prahl S 2002. Optical Absorption of Hemoglobin. In: Oregon Medical Laser Center.

Premereur E, Taubert J, Janssen P, Vogels R, Vanduffel W. 2016. Effective connectivity reveals largely independent parallel networks of face and body patches. Curr Biol. 26:3269–3279.

Raichle ME. 2015. The restless brain: how intrinsic activity organizes brain function. Philos Trans R Soc Lond B Biol Sci. 370: 20140172.

Reisman MD, Markow ZE, Bauer AQ, Culver JP. 2017. Structured illumination diffuse optical tomography for noninvasive functional neuroimaging in mice. Neurophotonics. 4:021102.

Rungta RL, Osmanski B-F, Boido D, Tanter M, Charpak S. 2017. Light controls cerebral blood flow in naive animals. Nat Commun. 8:14191.

Sanganahalli BG, Herman P, Blumenfeld H, Hyder F. 2009. Oxidative neuroenergetics in event-related paradigms. J Neurosci. 29:1707–1718.

Sato TR, Svoboda K. 2010. The functional properties of barrel cortex neurons projecting to the primary motor cortex. J Neurosci. 30:4256–4260.

Scott NA, Murphy TH. 2012. Hemodynamic responses evoked by neuronal stimulation via channelrhodopsin-2 can be independent of intracortical glutamatergic synaptic transmission. PLoS One. 7:e29859.

Shehzad Z, Kelly AM, Reiss PT, Gee DG, Gotimer K, Uddin LQ, Lee SH, Margulies DS, Roy AK, Biswal BB, et al. 2009. The resting brain: unconstrained yet reliable. Cereb Cortex. 19: 2209–2229.

Sheth SA, Nemoto M, Guiou M, Walker M, Pouratian N, Toga AW. 2004. Linear and nonlinear relationships between neuronal activity, oxygen metabolism, and hemodynamic responses. Neuron. 42:347–355.

Shmuel A, Leopold DA. 2008. Neuronal correlates of spontaneous fluctuations in fMRI signals in monkey visual cortex:

Implications for functional connectivity at rest. Hum Brain Mapp. 29:751–761.
Simons DJ, Woolsey TA. 1979. Functional organization in mouse barrel cortex. Brain Res. 165:327–332.
Smith SM, Fox PT, Miller KL, Glahn DC, Fox PM, Mackay CE, Filippini N, Watkins KE, Toro R, Laird AR, et al. 2009. Correspondence of the brain's functional architecture during activation and rest. Proc Natl Acad Sci USA. 106:13040–13045.
Stafford JM, Jarrett BR, Miranda-Dominguez O, Mills BD, Cain N, Mihalas S, Lahvis GP, Lattal KM, Mitchell SH, David SV, et al. 2014. Large-scale topology and the default mode network in the mouse connectome. Proc Natl Acad Sci USA. 111: 18745–18750.
Stark DE, Margulies DS, Shehzad ZE, Reiss P, Kelly AMC, Uddin LQ, Gee DG, Roy AK, Banich MT, Castellanos FX, et al. 2008. Regional variation in interhemispheric coordination of intrinsic hemodynamic fluctuations. J Neurosci. 28:13754–13764.
Taub AH, Katz Y, Lampl I. 2013. Cortical balance of excitation and inhibition is regulated by the rate of synaptic activity. J Neurosci. 33:14359–14368.
Thomson AM, Lamy C. 2007. Functional maps of neocortical local circuitry. Front Neurosci. 1:19–42.
Tolias AS, Sultan F, Augath M, Oeltermann A, Tehovnik EJ, Schiller PH, Logothetis NK. 2005. Mapping cortical activity elicited with electrical microstimulation using FMRI in the macaque. Neuron. 48:901–911.
Uddin LQ. 2013. Complex relationships between structural and functional brain connectivity. Trends Cogn Sci. 17:600–602.
Uddin LQ, Mooshagian E, Zaidel E, Scheres A, Margulies DS, Kelly AM, Shehzad Z, Adelstein JS, Castellanos FX, Biswal BB, et al. 2008. Residual functional connectivity in the split-brain revealed with resting-state functional MRI. Neuroreport. 19:703–709.
van den Heuvel MP, Bullmore ET, Sporns O. 2016. Comparative connectomics. Trends Cogn Sci. 20:345–361.
van Meer MP, van der Marel K, Wang K, Otte WM, El Bouazati S, Roeling TA, Viergever MA, Berkelbach van der Sprenkel JW, Dijkhuizen RM. 2010. Recovery of sensorimotor function after experimental stroke correlates with restoration of resting-state interhemispheric functional connectivity. J Neurosci. 30:3964–3972.
Vanni MP, Murphy TH. 2014. Mesoscale transcranial spontaneous activity mapping in GCaMP3 transgenic mice reveals extensive reciprocal connections between areas of somatomotor cortex. J Neurosci. 34:15931–15946.
Vazquez AL, Fukuda M, Crowley JC, Kim SG. 2014. Neural and hemodynamic responses elicited by forelimb- and photostimulation in channelrhodopsin-2 mice: insights into the hemodynamic point spread function. Cereb Cortex. 24: 2908–2919.
Veinante P, Lavallee P, Deschenes M. 2000. Corticothalamic projections from layer 5 of the vibrissal barrel cortex in the rat. J Comp Neurol. 424:197–204.
Vincent JL, Patel GH, Fox MD, Snyder AZ, Baker JT, Van Essen DC, Zempel JM, Snyder LH, Corbetta M, Raichle ME. 2007. Intrinsic functional architecture in the anaesthetized monkey brain. Nature. 447:83–86.
Wang H, Peca J, Matsuzaki M, Matsuzaki K, Noguchi J, Qiu L, Wang D, Zhang F, Boyden E, Deisseroth K, et al. 2007. High-speed mapping of synaptic connectivity using photostimulation in Channelrhodopsin-2 transgenic mice. Proc Natl Acad Sci USA. 104:8143–8148.
Weiler N, Wood L, Yu J, Solla SA, Shepherd GM. 2008. Top-down laminar organization of the excitatory network in motor cortex. Nat Neurosci. 11:360–366.
White BR, Bauer AQ, Snyder AZ, Schlaggar BL, Lee JM, Culver JP. 2011. Imaging of functional connectivity in the mouse brain. PLoS One. 6:e16322.
Wright PW, Archambault AS, Peek S, Bauer AQ, Culican SM, Ances BM, Culver JP, Wu GF. 2017a. Functional connectivity alterations in a murine model of optic neuritis. Exp Neurol. 295:18–22.
Wright PW, Brier LM, Bauer AQ, Baxter GA, Kraft AW, Reisman MD, Bice AR, Snyder AZ, Lee J-M, Culver JP. 2007b. Functional connectivity structure of cortical calcium dynamics in anesthetized and awake mice. PLoS One. 12 (10):e0185759.
Xiao D, Vanni MP, Mitelut CC, Chan AW, LeDue JM, Xie Y, Chen ACN, Swindale NV, Murphy TH. 2017. Mapping cortical mesoscopic networks of single spiking cortical or subcortical neurons. eLife. 6:e19976.
Yeo BT, Krienen FM, Eickhoff SB, Yaakub SN, Fox PT, Buckner RL, Asplund CL, Chee MW. 2015. Functional specialization and flexibility in human association cortex. Cereb Cortex. 25:3654–3672.
Yoshimura Y, Dantzker JLM, Callaway EM. 2005. Excitatory cortical neurons form fine-scale functional networks. Nature. 433:868–873.
Zhang D, Raichle ME. 2010. Disease and the brain's dark energy. Nat Rev Neurol. 6:15–28.